AGU PUBLICATIONS

JGR

Journal of Geophysical Research: Oceans

RESEARCH ARTICLE

10.1002/2015JC011011

DopSCAT: A mission concept for simultaneous measurements of marine winds and surface currents

Franco Fois[1,2], Peter Hoogeboom[1], François Le Chevalier[3], Ad Stoffelen[4], and Alexis Mouche[5]

[1]Faculty of Civil Engineering and Geoscience, Department of Geoscience and Remote Sensing, Delft University of Technology, Netherlands, [2]European Space Agency (ESA/ESTEC), Noordwijk, Netherlands, [3]Faculty Electrical Engineering, Mathematics, and Computer Science, Department of Microwave Sensing, Signals, and Systems, Delft University of Technology, Netherlands, [4]Active Remote Sensing Group, Satellite R & D, Royal Netherlands Meteorological Institute, de Bilt, Netherlands, [5]Department of Information Systems and Marine Data, Institut Français de Recherche pour l'Exploitation de la Mer, Brest, France

Key Points:
- Doppler scatterometry can provide simultaneous measurements of wind and currents
- The accuracy of sea current retrieval depends on the knowledge of marine wind measurements
- DopSCAT can improve our knowledge of ocean mesoscale dynamics

Correspondence to:
F. Fois,
F.Fois@tudelft.nl

Citation:
Fois, F., P. Hoogeboom, F. Le Chevalier, A. Stoffelen, and A. Mouche (2015), DopSCAT: A mission concept for simultaneous measurements of marine winds and surface currents, *J. Geophys. Res. Oceans*, *120*, 7857–7879, doi:10.1002/2015JC011011.

Received 30 MAY 2015
Accepted 4 NOV 2015
Accepted article online 6 NOV 2015
Published online 12 DEC 2015

Abstract A radar scatterometer operates by transmitting a pulse of microwave energy toward the ocean's surface and measuring the normalized (per-unit-surface) radar backscatter coefficient (σ°). The primary application of scatterometry is the measurement of near-surface ocean winds. By combining σ° measurements from different azimuth angles, the 10 m vector wind can be determined through a Geophysical Model Function (GMF), which relates wind and backscatter. This paper proposes a mission concept for the measurement of both oceanic winds and surface currents, which makes full use of earlier C-band radar remote sensing experience. For the determination of ocean currents, in particular, the novel idea of using two chirps of opposite slope is introduced. The fundamental processing steps required to retrieve surface currents are given together with their associated accuracies. A detailed description of the mission proposal and comparisons between real and retrieved surface currents are presented. The proposed ocean Doppler scatterometer can be used to generate global surface ocean current maps with accuracies better than 0.2 m/s at a spatial resolution better than 25 km (i.e., 12.5 km spatial sampling) on a daily basis. These maps will allow gaining some insights on the upper ocean mesoscale dynamics. The work lies at a frontier, given that the present inability to measure ocean currents from space in a consistent and synoptic manner represents one of the greatest weaknesses in ocean remote sensing.

1. Introduction

In the atmosphere, it is primarily heating that drives the global circulation and winds. The latter, in turn, determine the characteristics of the air-sea interaction and drive ocean surface currents together with the overturning circulation. Both the atmosphere and the ocean exhibit a complicated circulation pattern and their interaction determines much of the climate variability on time scales from several hours to seasons, years, decades, and millennia. Understanding this variability is essential to detect and predict climate change arising from external sources, such as solar irradiance variations and human activities. Improved knowledge of the dynamics of the global ocean circulation thus becomes imperative. An accurate prediction of climate conditions requires global measurements of the forcing of the ocean waters and of their motion. Ocean flows depend on aspects such as temperature and salt content, which together determine mass density and hence vertical movements. The ocean water flows include the major ocean currents which are continuous (with fluctuating velocity and position), medium, and small-scale circulation features (eddies), coastal, and tidal currents as well as waves generated by wind. Satellite altimetry has led to significant improvements in the understanding of the large-scale (>200 km) oceanic circulation [*Fu et al.*, 2010; *Zhang et al.*, 2007], providing unequalled views of the ocean eddy field and its kinetic energy on a global scale, and advance our understanding of ocean dynamics and its variability. Existing altimeters are capable of measuring large-scale changes in the ocean such as El Niño, La Niña, and sea level variations. However, the wide spacing of several hundred kilometers between the satellite ground tracks severely limits the cross-track resolution. As a matter of fact, Sea Surface Height (SSH) products have spatial resolution coarser than 100 km and temporal resolutions of about 10 days. Therefore, satellite altimetry data cannot resolve the small-scale (20–100 km) ocean eddies, which contain most of the energy and empower the mixing and

transport of water. These processes are important in determining how fast climate is changing. In the last years, new technologies have been developed in order to enhance future altimetric missions (namely SWOT [*Durand et al*., 2010] and WaveMill [*Gommenginger et al*., 2014] concepts), and on virtual constellation possibilities (e.g., Jason [*Bannoura et al*., 2005], CryoSat-2/SIRAL [*Galin et al*., 2013], SARAL/AltiKa [*Abdalla*, 2014], HY-2 [*Wang et al*., 2013], and Sentinel-3/SRAL [*Le Roy et al*., 2009]). Future ocean observing missions shall require global measurements of the important small-scale forcing, with revisit times (dictated by selected orbit and measurement geometry) sufficiently short to guarantee an adequate sampling of the associated processes. Eddies in the North Atlantic have typical radii of 20–50 km, amplitudes of 45 cm, and translational velocities of 2.5 km/day [*Fabry et al*., 2013]. This would require daily measurements with spatial sampling of 10–20 km. Consequently, observation requirements in terms of spatial resolution will certainly go even below 25 km resolution. For coastal applications, the constraints in terms of spatial resolution and revisit time are even more stringent thus challenging the performance of future ocean observing systems. Conventional interferometric techniques [*Romeiser and Thompson*, 2000] provide measurements of sea surface scatterer velocities by computing the phase difference among two return signals from the same point at two different times. It is also possible to measure sea surface velocities from estimates of the SAR Doppler anomalies [*Chapron et al*., 2003, 2005]. Although both techniques provide velocity products at high spatial resolution (of the order of kilometers), they have several disadvantages: the lack of global coverage due to frequent mode-switching and duty-cycle limitation, the poor temporal coverage, and the fact that only one component of the two-component surface current is mapped. In addition, the line-of-sight velocity depends on the wind field [*Chapron et al*., 2005; *Mouche et al*, 2008; *Johannessen et al*., 2008], which influence has to be correctly removed before the strength of the range-directed surface current can be determined. For SARs, this correction is possible only if the ocean wind vector is accurately known by other means. Scatterometers, on the other hand, with an antenna that provides multiple views, global ocean coverage and simultaneous wind vector estimation, appear, at first glance, to be ideal candidates for ocean surface current mapping using Doppler shift information. Nowadays, radar scatterometers are primarily designed to measure wind speed and direction from ocean radar backscatter, with spatial resolutions of tens of kilometers and swath widths wider than thousand kilometers. As these instruments were not specifically designed for Doppler measurements, new observation principles and data processing techniques must first be developed and validated. The combined availability of Ocean Vector Winds (OVW) and Ocean Vector Motion (OVM) would further allow a better comparison of earth-fixed atmospheric model or in situ observed winds and the ocean-relative winds from the scatterometer. Ocean winds are affected by currents and also by the temperature variations across ocean eddies which cause variations in atmospheric stability. Collocated OVW and OVM measurements would potentially resolve these effects. Starting from the principles of ocean Scatterometry, this paper presents an innovative microwave mission concept, called DopSCAT (Doppler Scatterometer), capable of resolving mesoscale features and their variations in time and space, with the objective of providing simultaneous worldwide measurements of OVW and OVM for operational use in weather and marine forecasting. Section 2 of this paper identifies the background and scientific issues to be addressed by Ocean Doppler Scatterometry, considering the contribution of past and present activities in the field. It provides a scientific justification for the mission, summarizes the specific research objectives of Doppler Scatterometry, and outlines the mission requirements, including required geophysical data products and observational parameters. Section 3 provides an overview of the system elements, including geometry, principle of observation and data processing. Section 4 makes a comparison of expected versus required performance and ability to fulfill the research/observational objectives based upon the documented system concept and validation approach.

2. User Product Requirements and Observing System Specifications

2.1. User Product Requirements

User requirements for ocean surface current measurements have been derived and presented in Table 1, based on outputs from an international User Consultation Meeting (UCM) by the ESA GlobalCurrent Project [*Donlon*, 2013]. The requirements are expressed as geophysical quantities with corresponding accuracy, spatial and temporal sampling, and coverage and length of data records. The majority of users request higher resolution products closer to the coast (1–2 km), 1–10 km for inland seas and 10–25 km spatial resolution for global products. Based on these user needs, our study shall target global coverage with a spatial

Table 1. Accuracy and Resolution Needs for Different Applications

Application	Coverage	Accuracy (cm s^{-1})		Spatial Resolution (km)		Temporal Resolution (h)		Length of Record (years)
		Threshold	Objective	Threshold	Objective	Threshold	Objective	
Weather service	Global	20	10	25	12.5	24	6	10+
Ocean service	Global	20	10	25	12.5	24	1	10
Search and rescue/coastguard	Regional	20	10	5	1	24	1	5
Scientific research	Regional	20	10	25	1	24	6	10
Marine renewable energy	Local	20	10	5	0.1	24	1	10
Pollution	Local	20	10	10	0.1	24	1	5
Sailing	Global	20	10	10		24		
Ship routing	Global	10	5	20	1	24	1	5
Wave forecasting	Global	20	10	25	2	24	0.5	1
Oil and gas	Local-Reg.	20	10	5	1	24	1	1
Marine offshore	Global	20	10	25	10	24	6	10
Fisheries management	Local	20	10	25	1	24	6	10

resolution of 10–25 km and higher resolution, where possible, at regional and local scales. Hourly products are required in tidal areas, if possible, and daily products as a minimum requirement for all areas. Table 1 reveals that a single year of data products is sufficient for demonstration purposes. A long-term archive of at least 10 years (preferably 20 years) is needed. The majority of users requires near real-time delivery of the products. The accuracy of the products is typically less than 0.20 m/s and independent on current regimes. Addressing the user needs set out in the previous section, requires repeated measurements of ocean currents at temporal and spatial scales compatible with the remote sensing mission. The envisaged remote sensing component is a C-band dual polarimetric Doppler Scatterometer mission, named DopSCAT. The DopSCAT instrument is a real-aperture fan-beam pulsed imaging radar operating at 5.4 GHz with six waveguide-array antennas configured in three antenna-pair assemblies similar to those of ESA's MetOp-ASCAT instrument [*Gelsthorpe et al*., 2000]. Each of the DopSCAT beams shall acquire a continuous image of the normalized (per-unit-surface) radar backscatter coefficient of the ocean surface, called σ°, and a continuous image of the ocean's Doppler shift over the swath. Both sides of the subsatellite track are imaged, each with three azimuth views, with an observation gap below the satellite. At each acquisition the radar will measure, simultaneously, the σ° and the ocean's Doppler shift. The measurements of the Doppler shift is possible by transmitting two chirps with opposite slopes (i.e., one up chirp and one down chirp) at the same time [*Fabry et al*, 2013], instead of a single chirp, as most of the wind scatterometers do. The received echoes are then processed on ground with two different matched filters, one adapted to the up chirp and the other to the down chirp, to generate two different images. The cross-correlation between these images provides accurate estimates of the ocean's Doppler shift. From the three different azimuth views, the OVM can thus be retrieved. The OVW is estimated using the classical processing of wind scatterometers. A large number of independent looks are summed in range and azimuth (multilooking), for each azimuth view, in order to achieve the specified radiometric resolution of the σ° estimate on each measurement pixel. The three σ° measurements (σ° triplet) are uniquely related to the 10 m vector wind through a Geophysical Model Function (GMF) [*Verhoef et al*., 2008; *Portabella and Stoffelen*, 2006]. The wind inversion is based on a search for minimum distance between the measured σ° triplet and simulated backscatter triplets lying on the GMF surface in the 3-D measurement space (space of triplets), taking into account instrumental and geophysical noise sources [*Portabella and Stoffelen*, 2006]. Due to measurement noise and the double harmonic wind direction dependence, multiple solutions are usually found (wind ambiguities), which have to be filtered out using background wind and wind error covariance information provided by a NWP model (ambiguity removal).

2.2. Observing System Specifications

2.2.1. Selection of Frequency

Historically, European and American scatterometers work at different bands. The European Space Agency uses C-band (5.3 GHz) and the National Aeronautics and Space Administration (NASA) uses Ku-band (14 GHz). At higher frequencies, short ocean waves have stronger influence on backscatter: this explains the higher sensitivity of Ku-band to low-winds. On the other hand, Ku-band is more affected by atmospheric effects. Clouds and rain can significantly attenuate the Ku-band signals. In addition, rain droplets distort the

gravity-capillary waves and this can complicate the wind vector retrieval. All these effects become smaller at lower frequencies. We note that the main ocean currents are associated with large SST gradients and therefore, often, with adverse weather. Considering the high technology readiness level of the main radar subsystems (e.g., antenna, radar electronics) and the extensive heritage in retrieving wind fields through the use of consolidated Geophysical Model Functions, both frequencies could in principle be suitable to DopSCAT. Although no technology nor performance limitations have been identified for the two bands, the C-band frequency has been retained for this study.

2.2.2. Polarization

Current operating scatterometers use only copolar scattering to retrieve wind speeds and directions. The main reason behind this design choice is associated with the fact that the Signal-to-Noise Ratio (SNR) in copolarization is expected to be higher than in cross polarization for most winds. However, airborne measurements over hurricanes, performed at C-band and Ku-band [*Fernandez et al*., 2006], have confirmed that copolar scattering suffers from problems of incidence and azimuth angle-dependent signal saturation and dampening, which make it only weakly sensitive to wind speed variations above 25 m/s. This shortcoming impairs the ability to provide accurate hurricane warnings. Recently, the analysis of RADARSAT-2 C-band multipolarization SAR data and collocated wind measurements by the NOAA Hurricane Hunter aircraft [*Fois et al*., 2014, 2015a; *Van Zadelhoff et al*., 2013; *Hwang et al*., 2010a, 2010b, 2014] have revealed that cross-polar scattering does not show any evident loss of sensitivity for wind speed well above 25 m/s, thus allowing accurate retrieval of strong-to-severe wind speeds. As a consequence, the use of cross polarization in addition to the most common VV polarization becomes imperative for proper hurricane forecasting with space-borne ocean scatterometers. The analysis of ocean Doppler shift anomalies measured by Envisat-ASAR [*Mouche et al*., 2012] have revealed that the ocean Doppler spectrum at microwave frequencies can be different for different polarizations. Copolar scattering experiences Doppler frequency shifts higher than the cross-polar scattering. The Doppler shift increases with the wind speed. The rate of this increase depends on the wind directions: as we approach the cross-wind direction, the wind speed sensitivity gets weaker. Geophysical Model Functions such as SSA2-CWM [*Fois et al*., 2015b] and CDOP [*Mouche et al*., 2012] can be used to identify the wind contribution to the sea surface velocity, thus making the observation of ocean currents possible. The preferred polarization for measuring ocean currents is VV, because of the highest signal-to-noise ratio, which has a direct impact on the accuracy of the ocean motion vector retrieval.

2.2.3. Incidence Angle

The incidence angle of the instrument affects both electromagnetic scattering and Doppler signature from the ocean. Typical incidence angles for ocean application range between 20° and 65°. Below 20° the wind directional sensitivity is very poor, whereas above 65° the link-budget performance of the radar are strongly degraded, because of the very long slant range distances involved and the low values of the normalized radar cross section, which decreases with the incidence angle. On the other hand, in order to obtain clear measurements of surface current variations, the incidence angles should be as high as possible. In fact, high incidence angles reduce the relative contribution of vertical components of wave motions to the Doppler signature of the ocean.

2.2.4. Revisit Requirements

As outlined in section 2.1, most of the applications require global coverage in 24 h. This imposes constraints on the swath width and correspondingly on the antenna design, the level of transmit power, and the radar instrument timing. With the incidence angle range adopted for DopSCAT (from 20° to 65°), 99% of the Earth is covered within 48 h, whereas 87% of the Earth is covered within 24 h.

2.2.5. Doppler Measurement Capability

The DopSCAT system has to perform Doppler measurements in addition to backscattering measurements. This requirement imposes constraints on the type of waveform to be transmitted, on the instrument timing and on the data processing.

2.2.6. Spatial Resolution and Sampling

In technical terms, the single-look resolution of a scatterometer is limited by the bandwidth of the transmit signal and by the antenna length. Although, single-look data have high resolution, they are impractical to work with, as they are characterized by a large speckle noise. Speckle arises from interference between the different scatterers within a single resolution cell. To reduce this uncertainty, radar intensity images are typically incoherently averaged. The number of independent samples in the average is known as the equivalent number of looks. In section 2.1, we have pointed out that the resolution required to meet the DopSCAT mission objectives is between 10 and 25 km on global scale. Accordingly, two types of products can be defined:

a nominal product with spatial resolution of 25 × 25 km^2 and spatial sampling of 12.5 km, along with a high-resolution product with spatial resolution <12.5 × 25 km^2 (across-track × along-track) and spatial sampling of 6.25 km.

2.2.7. Radiometric Resolution (k_p)

In scatterometry, it has become customary to define the measurement error in terms of the so called k_p parameter, which is the normalized standard deviation of the measurement error or percentage error. A goal of scatterometer design is the minimization of k_p. The k_p requirement drives the antenna elevation pattern shape, the average transmitted power and the modulation parameters of the transmit signal. For a homogeneous scene, the radiometric resolution can be expressed as:

$$k_p = \sqrt{\frac{1}{N_A N_R}\left(1+\frac{1}{\left(\frac{S}{N}\right)^2}\right)+\frac{1}{N_N}\left(\frac{1}{\left(\frac{S}{N}\right)^2}\right)}, \tag{1}$$

where N_A and N_R are the number of independent along-track and across-track looks, whereas N_N is the number of independent noise looks. The quantity S/N is the Signal-to-Noise Ratio (SNR). The radiometric resolution for the nominal products in VV and VH-polarization shall be compliant with the following specifications, corresponding to different wind scenarios:

1. VV-pol at 4 m/s crosswind: $k_p \leq 3\%$ for $\theta_i \leq 25°$; $k_p \leq (0.175 \times \theta_i - 1.375)$ % for $\theta_i > 25°$;
2. VV-pol at 25 m/s upwind: $k_p \leq 3\%$;
3. VH-pol at 15 m/s crosswind: $k_p \leq 15\%$;
4. VH-pol at 40 m/s upwind: $k_p \leq 5\%$;

where θ_i represents the incidence angle. The analytical full-polarimetric scattering model SSA2-CWM [*Fois et al*., 2015a,b] together with the empirical models CMOD5n [*Verhoef et al*., 2008] and VH-GMF [*Van Zadelhoff et al*., 2014] will be used in this paper as geophysical model functions for the transfer between vector wind and backscattering coefficient of the ocean. *Portabella* and *Stoffelen* [2006] discussed inhomogeneous scenes, but this is not elaborated here.

2.2.8. Radiometric Bias and Stability

Two main radiometric parameters are defined for the DopSCAT mission: the Radiometric Bias (RB) and the Radiometric Stability (RS). The combination of these two quantities provides the Radiometric Accuracy (RA), describing the total error in the measurement of $\sigma°$. The Radiometric Bias is defined as the bias in the measured radar cross section of a calibration target over the mission lifetime. Correction for this bias (absolute calibration) is unlikely to be critical, as it can be compensated for in the retrieval of geophysical quantities. It becomes relevant principally when comparing data from different reference targets or when DopSCAT's data are compared with data from other C-band instruments. A threshold of 0.4 dB (at 1 sigma) is considered adequate, since such constant offsets can be dealt with by cross calibration. The Radiometric Stability is defined as the standard deviation of measurements of the radar cross section of an unsaturated invariant target, taken at different times. This is critical for a wind scatterometer as the wind vector retrieval relies on the stability of the relationship between backscatter and wind field. A radiometric stability of 0.1 dB (at 1 sigma) is considered for DopSCAT.

3. Measurement System Concept

Failure in several attempts to accurately estimate surface current information from radar Doppler shift can be attributed, in a large part, to the assumption that the geophysical source of Doppler shift over ocean surface is only the surface current. *Chapron et al*. [2003, 2005] showed that sea state contributes significantly to the Doppler shift. This contribution can be estimated, in average, by using surface wind vector information. The relatively small-scale scattering elements in the sea state, that are the steepest and the major contributors to the Doppler shift, are generally in local equilibrium with the surface wind. The measured geophysical ocean motion vector can thus be expressed as:

$$\mathbf{v}_{OVM} = \mathbf{v}_O^{wind} + \mathbf{v}_O^{curr} + \mathbf{v}_O^{\text{int}}. \tag{2}$$

These terms represent the contributions to the OVM associated with the wind, $\mathbf{v}_O^{wind}$, the ocean current, $\mathbf{v}_O^{curr}$, and wind-wave-current interactions, $\mathbf{v}_O^{\text{int}}$. The wind-driven term includes the motion due to the larger-scale metric waves together with Stokes drift, wind drift, short-wave motions, and nonlinear hydrodynamic

modulations of short waves by large waves. The relative difference between the Doppler shifts of sea state and the surface current is larger at small incidence angle (below 30°), where the motion is dominated by large-scale gravity waves which propagate faster. As the incidence angle increases, hydrodynamic modulations of short waves by large waves become the dominant contribution to the Doppler velocity. An interesting property of the sea state Doppler shift is that it depends on the polarization, especially at large incidence angles (above 30°) and therefore simultaneous observations at HH and VV polarizations could, in principle, be helpful to independently characterize this sea state contribution. In our study, sea state/surface current interactions, that can be large in area of strongly varying surface current over short distances, are neglected. We assume that, at a resolution of a tens of kilometers (typical of ocean scatterometers) these rapidly varying surface currents are averaged out. Therefore, a simplified relationship between the sea surface current and the ocean motion vector is:

$$\mathbf{v}_O^{curr} = \mathbf{v}_{OVM} - \mathbf{v}_O^{wind}. \tag{3}$$

Of course, this assumption will become questionable in coastal areas where surface current can be dominated by tidal currents modulated by complex bathymetry. However, for global ocean monitoring, this should be an acceptable assumption. In [*Chapron et al*., 2005, Figure 5], the use of the ENVISAT's ASAR continuous Wave Mode data enabled to stress the strong signature of the atmospheric circulation in the Doppler measurements. The joint distribution of the observed Doppler anomalies and collocated surface winds given by the European Centre for Medium-Range Weather Forecasts (ECMWF) showed that, at first order, the sea state induced by the surface wind dominates the Doppler measurements. As for the NRCS, for a given sea state the Doppler shift is expected to be dependent on the radar configuration (frequency, polarization, incidence, and azimuth angle). Several theoretical studies have been proposed to better understand the contribution of ocean waves to the Doppler shift. The question is still open but it appears rather clear that the multiscale property of the sea surface has to be taken into account to fully understand the characteristics of the microwave signal [*Romeiser and Thompson*, 2000; *Johannessen et al*., 2008; *Mouche et al*., 2008]. To complement these physically based studies, systematic colocations between ENVISAT ASAR's data in Wide Swath mode and ASCAT winds within 30 min of acquisitions have been collected in geographical areas free of strong sea surface currents. The use of the WS (Wide Swath) data enabled to investigate the relationship between the Doppler and the incidence angle with respect to the surface wind speed and direction. The idea of such a work was to derive a simple geophysical function (CDOP) for the Doppler anomaly with respect to radar configuration and wind vector. This model relates the Doppler measurement at C-band in VV and HH polarizations to the incidence angle, the wind speed and the relative wind direction to the antenna look angle. The Doppler shift is expected to be zero when the wind is blowing in the azimuth direction and maximal (respectively minimal) when it blows toward (away from) the antenna. Within the range of incidence angles 17°–45°, the impact of the sea state on the Doppler decreases when the incidence angle increases. This empirical GMF was routinely used to correct the ASAR Doppler grid from the sea state contribution in areas where strong currents are expected (e.g., Agulhas and Gulf Stream). Recently, an analytical model for the description of the full-polarimetric sea surface scattering and Doppler signature has been derived [*Fois et al*., 2015b] by combining the Small Slope Approximation theory (at the second-order) with the nonlinear Choppy Wave Model transformation of the linear sea surface. Being based on a description of the underlying physical phenomenon, this analytical model have the big potential of providing a more general and understandable relation between measured microwave ocean signatures (i.e., scattering and Doppler) and surface wind field than the empirical models. Considering the extended capabilities (e.g., larger incidence angle range, better spatial resolution, multipolarization observation capabilities) of DopSCAT as opposed to present and past scatterometers, the SSA2-CWM geophysical model function represents a very powerful tool that can support the design of the DopSCAT mission by extending the boundaries of CMOD and CDOP GMFs.

3.1. Sea Surface Representation

The 2-dimensional properties of the sea surface determine the characteristics of both measured NRCS and Doppler signature. Today, one of the most well-known and accepted spectral models is the *Elfouhaily* unified spectrum [*Elfouhaily et al*., 1997]. Very recently, an improved spectral model for short waves has been proposed in *Hwang et al*. [2013] and *Hwang and Fois* [2015], where a method is developed to obtain the short-scale properties of ocean surface roughness and wave breaking from Ku, C, and L band polarimetric sea returns. The results are used for quantitative evaluation of the ocean surface roughness spectral models

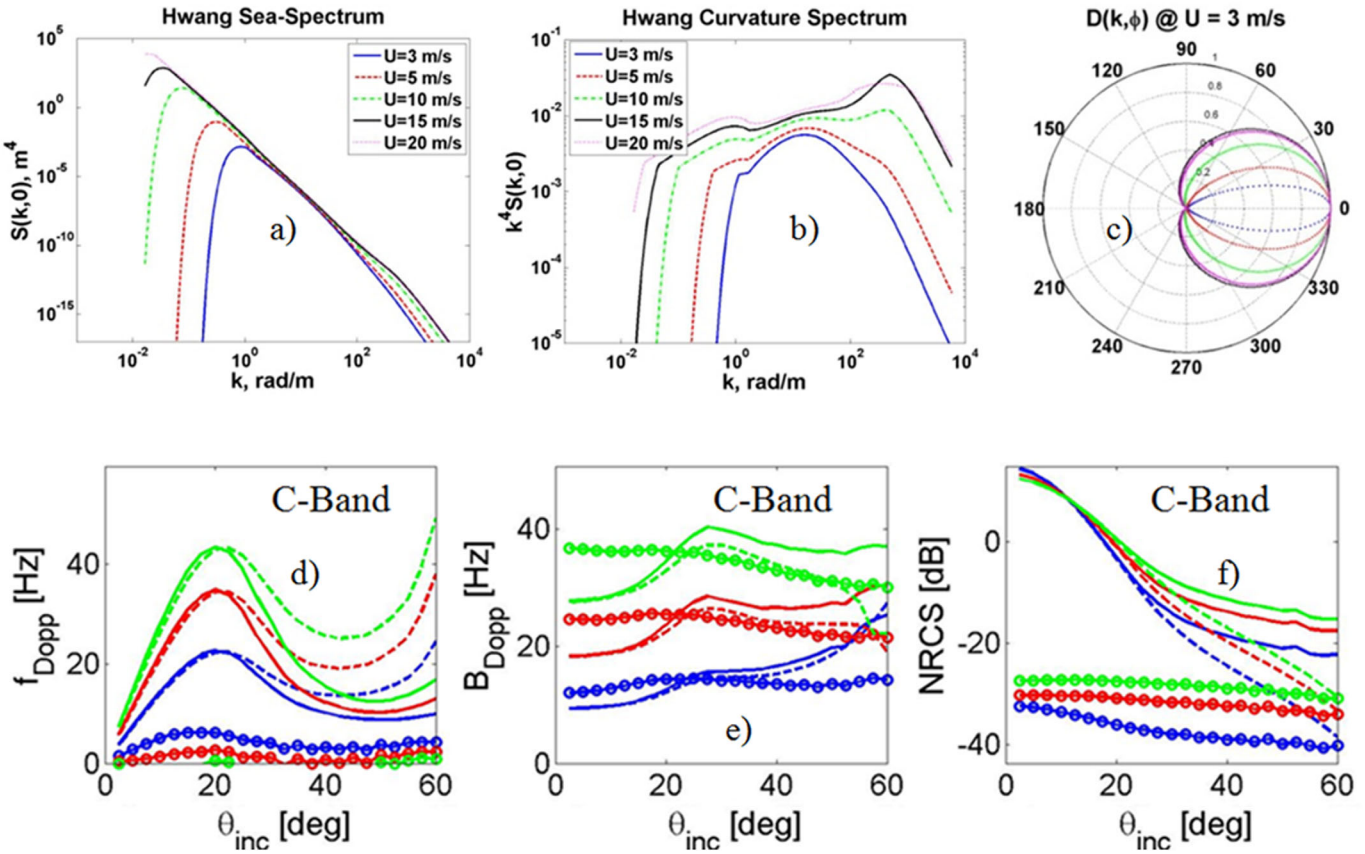

Figure 1. (a)–(c) Hwang spectrum at various wind speeds and fetches of $9.7U^2$ km. (a) The wave height variance spectral density in the direction of the wind; (b) the curvature spectrum in the wind direction; (c) the angular part of the spectrum, $D(k,\Phi)$. The different lines, here, show, in order of increasing loop size $k/k_p = 1, 3, 10, 50$, while the line in magenta corresponds to $k/k_p = 1000$. (d)–(f) Doppler shift, Doppler bandwidth, and NRCS computed by SSA2-CWM at C-band: green lines refer to 13 m/s wind speed (upwind), whereas the red and blue lines refer to 9 and 5 m/s, respectively. In the figures, dashed lines are used for HH, solid lines for VV and circles for VH.

and for deriving understanding of the breaking contribution, in particular its dependence on wind speed, microwave frequency, and incidence angle. The *Hwang* ocean wave height, curvature spectra, and spreading function are shown in Figures 1a–1c for various wind speeds and fetches. In remote sensing applications, the sea surface height is often modeled with Gaussian statistics. This representation of the ocean sea surface is called linear. However, nonlinear surface waves can have an important impact on the interpretation of scattering data. The deviations from the Gaussian law of the slope distribution may have a visible impact on the radar returns. Nonlinear hydrodynamics link the motion of the large and small waves and modify both shape and statistical characteristics of the ocean sea surface. Hydrodynamic modulations of short waves by large waves are identified [*Plant*, 2002] as one of the reasons for the directional variation of the radar return and the observed difference among upwind and downwind measured NRCS. Most of the nonlinear models [*Hasselmann*, 1962; *Longuet-Higgins*, 1963] are only applicable to long gravity waves. For shorter waves, instead, wave-wave interactions to higher-order become nonnegligible and must be accounted for. A numerically efficient weakly nonlinear model was developed recently by *Nouguier et al.* [2009]. It is called Choppy Wave Model (CWM) and is based on the nonlinear transformation of a reference linear surface. This transformation is performed through a horizontal shifting process of waves that makes them look choppy. The model provides a statistical formulation of the ocean surface in terms of sea surface height/slope distributions, associated higher-order moments and joint-probabilities.

3.2. Sea Surface Scattering and Doppler Signature

In this paper, the Choppy Wave Model is combined with the second-order Small Slope Approximation [*Voronovich*, 1994] to describe the full-polarimetric sea surface scattering and Doppler signature. Results obtained by *Fois et al.* [2015b] at different frequencies (C, X, and Ku-bands) show that the predicted wind-induced Doppler shift is larger in HH than in VV polarization. The radar signal is, in fact, more sensitive to

the smaller waves in VV polarization than in HH. On the contrary, the radar signal is more sensitive to larger propagating waves in HH polarization than in VV polarization. Shorter gravity ocean waves are slower, whereas larger propagating waves are faster. As compared to the copolar signals, the cross-polarized backscatter experiences a much lower Doppler shift across the full range of incidence angle investigated, due to its different scattering properties. The Doppler shift of the cross polarization looks less sensitive to wind speed variations than the copolarization. The central Doppler frequency for the copolar signal shows an evident peak around 22° incidence, whereas this peak is not visible in VH polarization. At small incidence angles, linear and nonlinear Doppler spectra almost coincide, because the influence of the horizontal velocity component on the Doppler spectrum is small. As the incidence angle increases, nonlinear sea surfaces show larger Doppler central frequency and Doppler spread than the corresponding linear sea surfaces (i.e., Gaussian distribution of sea surface heights). This happens because the Choppy Wave Model corrects the horizontal component of particle velocities by adding a displacement, related to the surface elevation, to the horizontal position of the particles. Numerical results obtained by using the SSA2-CWM model are in good agreement with real measurements from ENVISAT-ASAR and SAXON-FPN Ku-band campaign [*Plant and Alpers*, 1994]. The results are also consistent with the empirical Geophysical model function CDOP. Figures 1d–1f show the Doppler shift, the Doppler Bandwidth, and the NRCS computed by SSA2-CWM at C-band: green lines refer to 13 m/s wind speed (upwind), whereas the red and blue lines refer to 9 and 5 m/s, respectively. In the figures dashed lines are used for HH, solid lines for VV and circles for VH. To validate the second-order Small Slope Approximation, we have compared the NRCS of the model with real measurements from different data sets, namely Sentinel-1 Extra Wide Swath ocean data set and ENVISAT-ASAR ocean data sets. Figures 2a–2f show the cloud of ASAR normalized radar cross-section measurements in VV polarization versus collocated (close enough in space and time to be representative) wind speed measurements provided by the MetOp-ASCAT scatterometer. The following incidence angles are analyzed: 20°, 24°, 28°, 33.5°, and 39.5°. For each wind speed, the NRCS values associated with all possible wind directions are plotted. The different colors in the two figures represent the frequency of the observations. Black and gray lines represent the NRCS computed by using the SSA2 model in combination with *Hwang* and *Elfouhaily* sea surface spectrum, respectively. The magenta lines show the backscattering coefficients given by the geophysical model function CMOD5n. Solid and dashed lines correspond to upwind and crosswind cases, respectively. The use of the *Hwang* spectrum over estimates the VV-pol NRCS of about 1–2 dB at low incidence angles ($<$20°) and wind speeds above 10 m/s. Although the *Elfouhaily* unified directional wave spectrum matches better the ASAR data in upwind cases, it underestimates the crosswind cases of about 1–3 dB within the wind speed range 3–15 m/s. The CMOD5n geophysical model function should well represent the transfer between vector wind and backscattering coefficient of the ocean, as it is built on the basis of a collocation between MetOp-ASCAT backscatter triplets and ECMWF first-guess winds. However, some discrepancies are visible at 20° incidence. In fact, CMOD5n seems to underestimate the NRCS of 1–2 dB in upwind cases. These discrepancies can be justified by the fact that the validity of CMOD5n is limited to the incidence angle range 25°–55°, corresponding to near and far swath of the ASCAT scatterometer. For incidence angles higher than 20°, the agreement between the SSA2 model and the cloud of VV-polar measurements significantly improves and the differences between model and measurements are in the order of 1 dB or less, except for very low wind speeds ($<$4 m/s) for which the measurement accuracy is affected by the limited radiometric resolution. The Hwang spectrum shows a better match with the measurements than both *Elfouhaily* spectrum and the empirical model function. This is particularly evident in crosswind and high incidence angles. Figures 2g–2i show the clouds of VV-polar measurements by ASAR collected, as function of the wind direction, within different incidence angle ranges (30°–32°, 33°–35°, 36°–38°, 39°–41°) and corresponding to wind speeds between 5 and 10 m/s. Overlaid are the simulated NRCS obtained by using the SSA2 model with the *Hwang* wave height spectrum: Solid and dashed lines refer to 10 and 5 m/s wind, respectively. For each wind speed, two curves are plotted, corresponding one to the minimum and the other to the maximum angle within the observed range. The modulation of the measured VV-NRCS with the wind direction is well predicted by the SSA2 model. Figure 3 shows the cloud of Sentinel-1 measurements in HV-polarization versus ECMWF forecasted wind for different incidence angle ranges (20°-23°, 29°-33.5°, 34.5°-38.5°, 43.75°-46°). The colors represent the frequency of observations. The black solid and dashed lines show the *Vachon and Wolfe* [2011] and the *Zhang et al* [2014] empirical model functions. The magenta lines depict the SSA2 model computation, with *Hwang* spectrum, at the extreme angles of the observed areas: in particular solid magenta lines refer to upwind cases at the lowest incidence angles

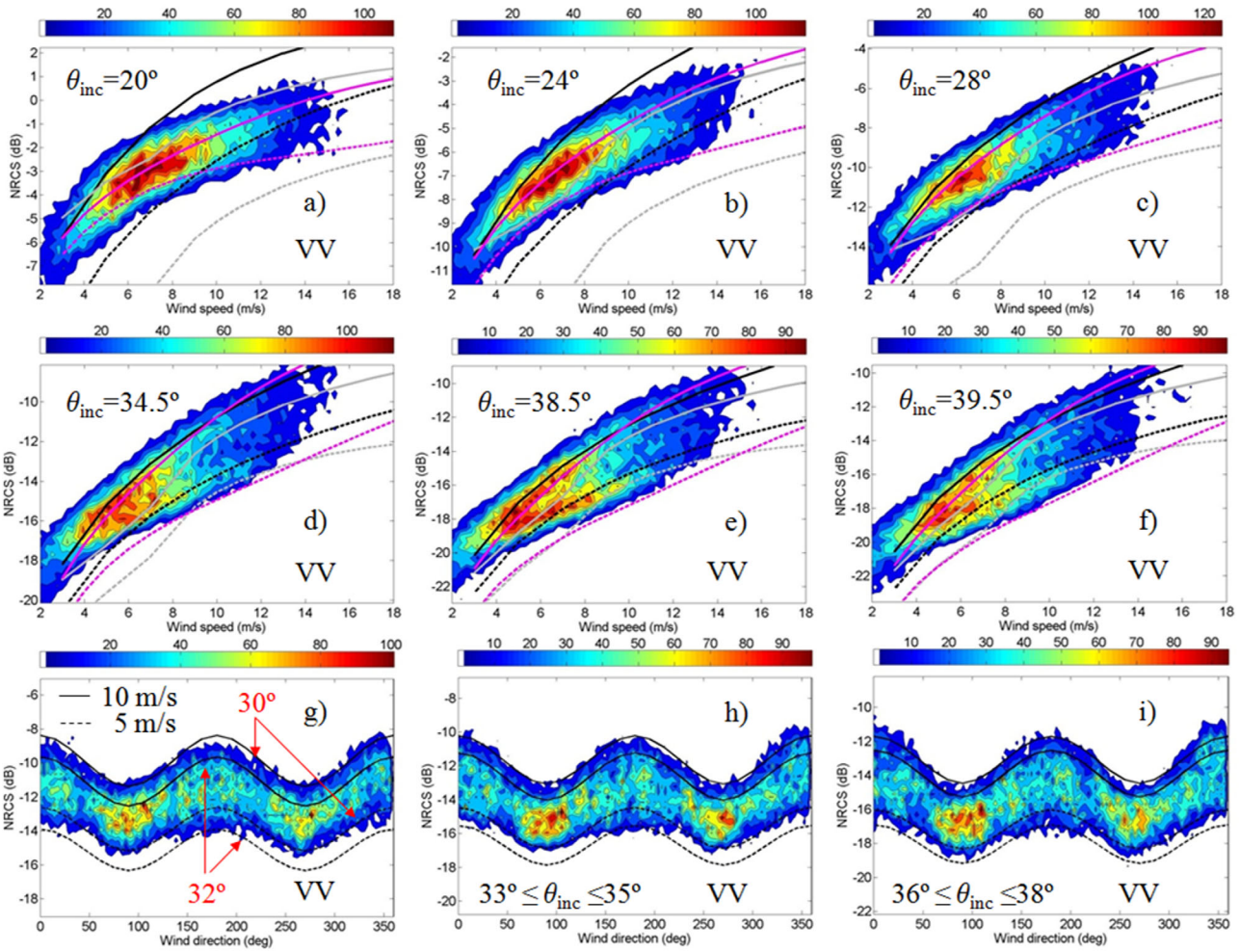

Figure 2. (a)–(f) Two-dimensional histograms of the NRCS in VV polarization versus wind speed for different incidence angles (20°, 24°, 28°, 34.5°, 38.5°, 39.5°). Black curves correspond to numerical calculations performed with SSA2 and Hwang spectrum. Gray curves correspond to SSA2 and Elfouhaily spectrum. Magenta curves correspond to CMOD5n geophysical model function. Solid lines depict upwind cases whereas dashed lines depict cross-wind cases. (g)–(i) Clouds of ASAR measurements collected in VV-polarization at different incidence angle ranges (30°–32°, 33°–35°, 36°–38°) and corresponding to wind speeds between 5 and 10 m/s. Overlaid are the SSA2 simulated NRCS: Solid lines refer to 10 m/s wind (at minimum and maximum incidence angles within the observed range), whereas dashed lines refer to 5 m/s (at minimum and maximum incidence angles).

whereas dashed magenta lines correspond to crosswind cases at the highest incidence angles. The gray lines, instead, depict the SSA2 model computation, with *Elfouhaily* spectrum, at the extreme angles of the observed areas. Green and red dots show the RADARSAT-2 measurements in Quad-Pol mode with and without noise correction: these dots are used as a reference. Only Sentinel-1 data with adequate signal-to-noise ratios have been considered: they correspond to the center of the swaths where the expected NESZ values are between −28 and −34 dB. Within the wind speed range 5–15 m/s, the agreements between SSA2 model and measurements is better than 2 dB. Numerical computations of the SSA2 model with *Elfouhaily* and Hwang spectrum show some systematic difference:

1. Within the wind speed range 5–8 m/s, the *Elfouhaily* spectrum slightly underestimates VH-NRCS;
2. Below 5 m/s the cross-polar scattering estimates associated with the two spectra are comparable;
3. Above 10 m/s and up to 25 m/s, the *Hwang* spectrum shows a better match with the measurements than the *Elfouhaily* one. Differences between the two spectra can reach up to 2.5 dB;
4. Above 10 m/s, the rates of increase of NRCS versus the wind speed in upwind and crosswind cases are slightly different for the *Hwang* spectrum, whereas they are about the same for the *Elfouhaily* spectrum.

A clear mismatch is visible between Sentinel-1 and RADARSAT-2 noise corrected data at 20° and 24° incidence: the cross-polar backscattering coefficient for RADARSAT 2 is, in fact, systematically lower than for

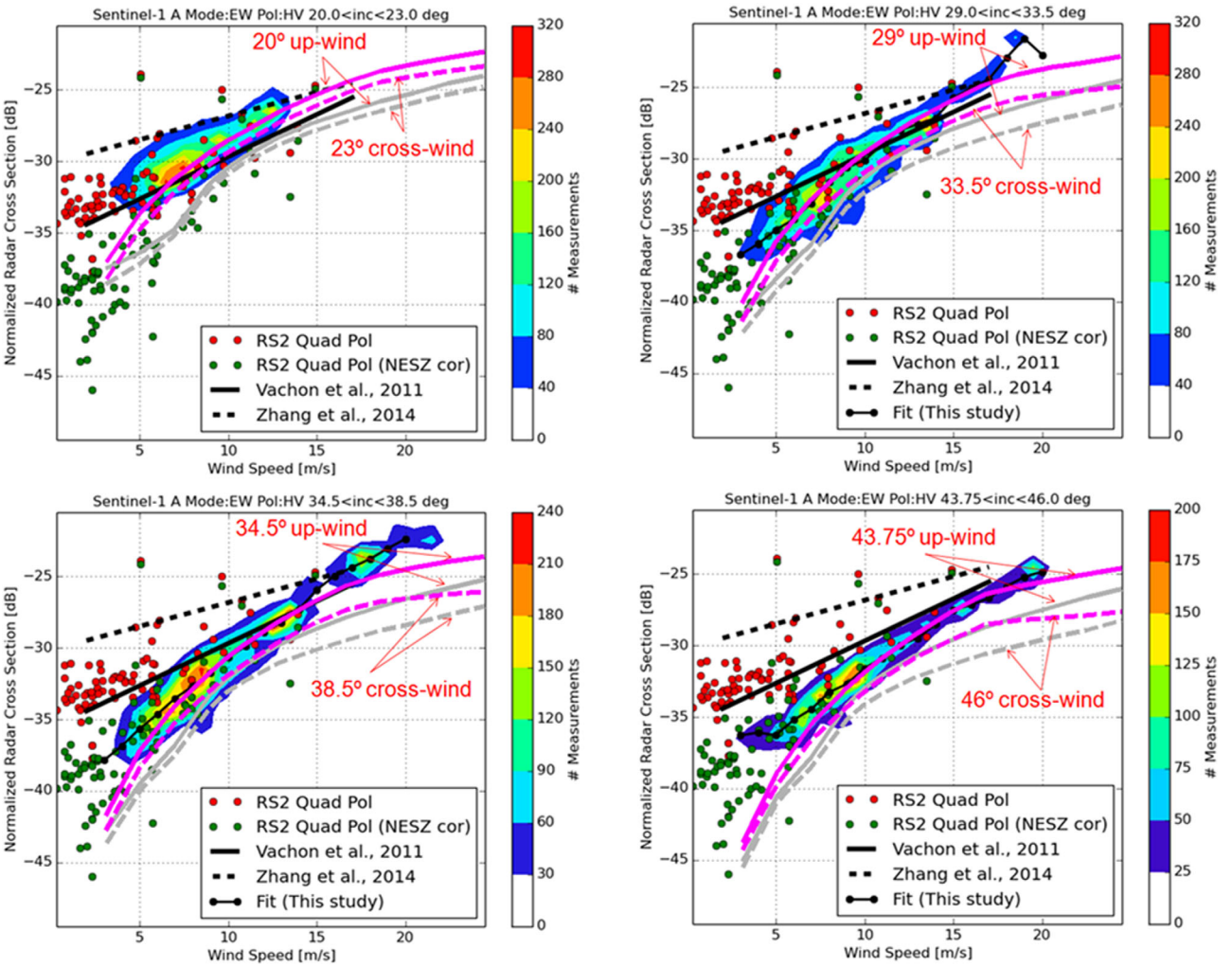

Figure 3. Cloud of Sentinel-1 measurements in HV-pol versus ECMWF wind for different incidence angle ranges (20°-23°, 29°-33.5°, 34.5°-38.5°, 43.75°-46°). The colours represent the frequency of observations. Magenta and gray lines correspond to SSA2 model combined with Hwang and Elfouhaily spectrum, respectively.

Sentinel-1. This effect is more evident at low wind speed and almost disappears above 29°, where the RADARSAT 2 measurements are found more consistent with Sentinel-1 data.

3.3. Orbit Selection and Geometry of Observation

The sun-synchronous orbit of the MetOp satellites has been chosen for the DopSCAT mission. The geometry of observation of the DopSCAT instrument is depicted in Figure 4. Six swaths are alternatively illuminated on ground by six fixed fan beam-antennas, with a time sampling dictated by the pulse repetition frequency of the radar. The swaths are oriented at 45° (Fore-left), 90° (Mid-left), 135° (Aft-left), 225° (Aft-right), 270° (Mid-right), and 315° (Fore-right) with respect to the satellite ground track. Mid swaths extend from 20° incidence up to 53.75°, whereas side swaths extend from 27.42° incidence up to 65°. This corresponds to an overall performance swath of 660 km on both sides of the subsatellite ground-track, with a gap of 525 km in between. Such a swath ensures a 99% global coverage in 48 h.

3.4. Observation Principle

Linearly frequency-modulated pulsed signals (chirps) are commonly used by radar systems, as they have significant advantages with respect to CW-pulsed signals. The range resolution of a CW-radar system depends on the pulse duration: the shorter the transmit pulse the better the resolution, with a corresponding limitation in average radiated power and sensitivity. For chirp signals, however, the range resolution depends on the bandwidth of the transmit waveform: the larger the bandwidth the higher the resolution,

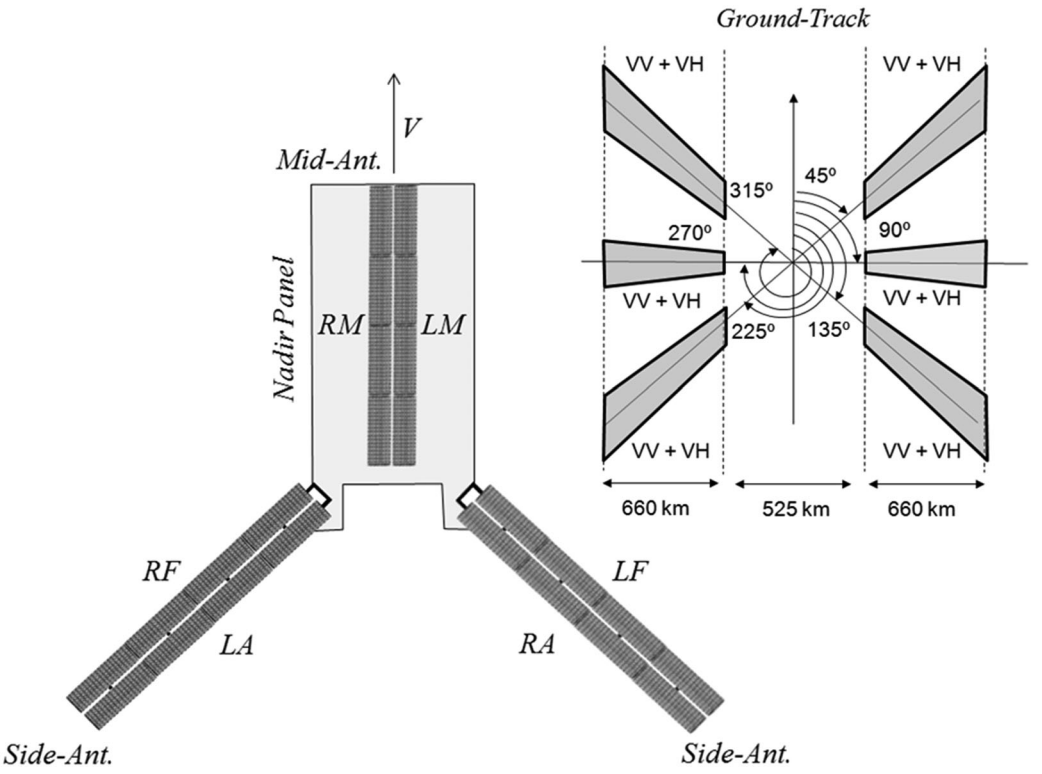

Figure 4. Geometry of observation. Six waveguide array antennas are used to observe six swaths on ground (three on each side of the sub-satellite ground track). The terms RF, LA, RA, LF, MR, and ML stand for Right-Fore, Left-Aft, Right-Aft, Left-Fore, Mid Right, and Mid Left antennas, respectively.

without any relation to the pulse length or average radiated power. For DopSCAT, the transmitted signal is a dual chirp, a combination of two linear frequency modulated pulses: one with increasing frequency, i.e., up chirp, and the other with decreasing frequency, i.e., down chirp. Up and down chirps are transmitted at the same time and have the same bandwidth (B) and pulse duration (τ):

$$s(t)=s_u(t)+s_d(t)= \\ =\left\{A\exp\left[j2\pi\left(f_c t+\frac{1}{2}\frac{B}{\tau}t^2\right)\right]+A\exp\left[j2\pi\left(f_c t-\frac{1}{2}\frac{B}{\tau}t^2\right)\right]\right\}\ \mathrm{rect}_\tau(t). \tag{4}$$

In equation (4), the subindexes u and d stand for "up-chirp" and "down-chirp", respectively, f_c is the carrier frequency and A is an arbitrary amplitude factor, rect_τ is a rectangular function of duration τ. The use of dual chirps allows estimating not only the backscattering coefficient of the wind-driven ocean surface but also the Doppler shift associated with the moving ocean. The demonstration of this capability can be based on the radar ambiguity function. In a radar system, the choice of a radar waveform plays an important role in enabling the system to separate two closely located targets, in either range or speed. Therefore, it is often necessary to examine a waveform and understand its resolution and ambiguity in both range and speed domains. In radar, the range is measured using the delay and the speed is measured using the Doppler shift. Thus, the range and the speed are used interchangeably with the delay and the Doppler. To improve the signal to noise ratio (SNR), modern radar systems often employ a matched filter in the data processing. The ambiguity function of a waveform represents exactly the output of the matched filter when the specified waveform is used as the filter input, that is:

$$\chi(\tau_s, f_D)=\int_{-\infty}^{\infty} s(t)\cdot s^*(t-\tau_s)\cdot e^{j2\pi f_D t}dt, \tag{5}$$

where * denotes the complex conjugate, τ_s the time delay, and j is the imaginary unit. Note that for zero Doppler shift ($f_D=0$) this reduces to the autocorrelation of $s(t)$. This exact representation makes the

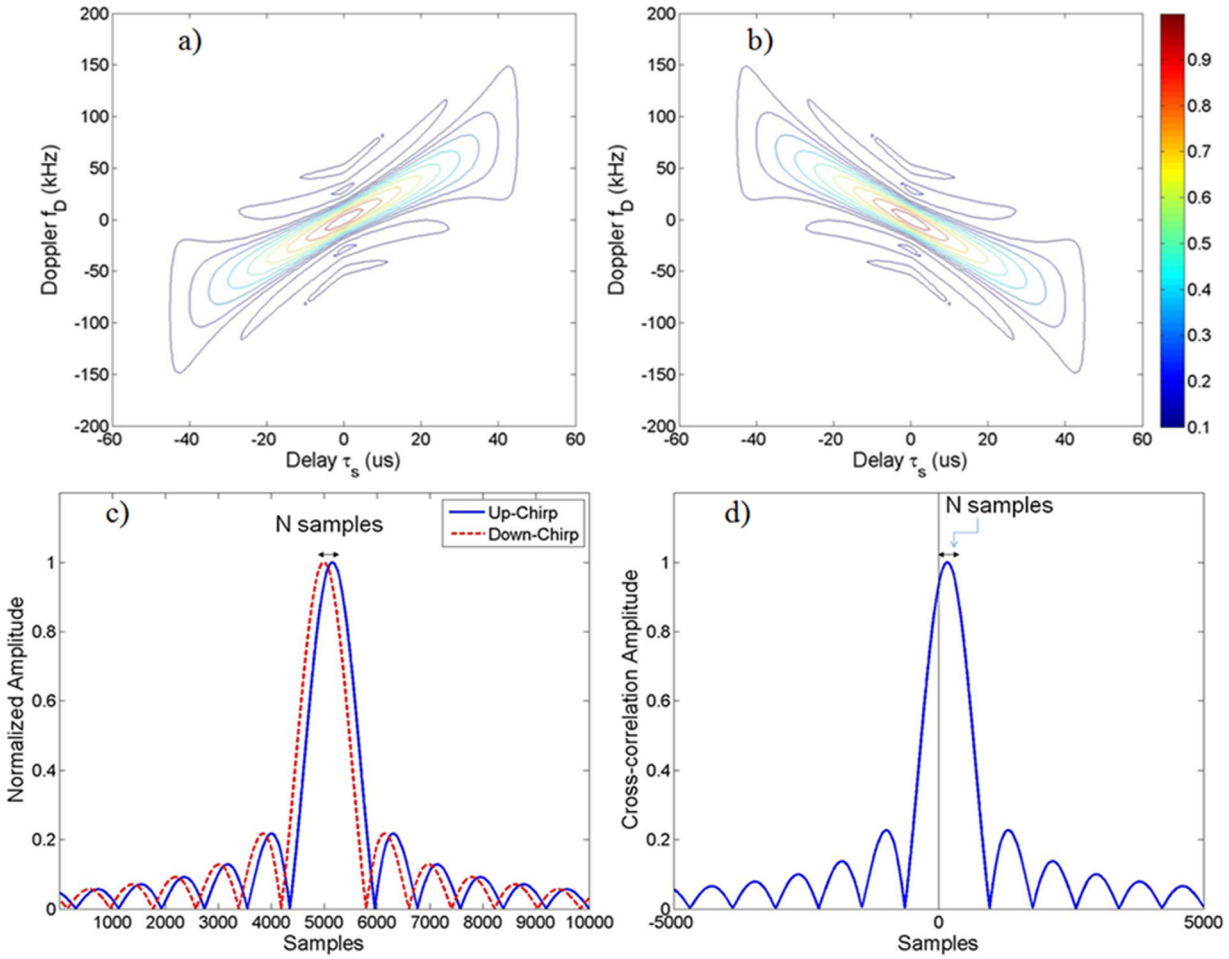

Figure 5. The ambiguity function of, (a) an up chirp and, (b) a down chirp LFM pulse. (c) relative time delay between two LFM pulses with opposite rates subjected to a common Doppler shift and (d) result of the cross correlation.

ambiguity function a popular tool for designing and analyzing waveforms. This approach provides the insight of the resolution capability in both delay and Doppler domains for a given waveform. Based on this analysis, one can then determine whether a waveform is suitable for a particular application. A constant envelope Linearly Frequency-Modulated (LFM) pulse has an ambiguity function skewed in the delay-Doppler plane. In the matched filter output slight Doppler mismatches for the LFM pulse do not change the general shape of the pulse and reduce the amplitude very little, but they do appear to shift the pulse in time. Thus, an uncompensated Doppler shift changes the target apparent range; this phenomenon is called range-Doppler coupling. Figure 5 uses the ambiguity function to explore the range-Doppler relationship for a Linear Frequency Modulated Pulse. In particular, Figure 5a depicts the up chirp (positive chirp rate) case and Figure 5b the down chirp (negative chirp rate) case. The ambiguity functions of LFM pulses with opposite chirp rates are skewed in opposite direction, meaning that the introduced delay has an opposite sign. While one return appears delayed the other one of the same quantity appears earlier. The delay is proportional to the Doppler shift and inversely proportional to the chirp rate:

$$\tau_s = f_D \cdot \left(\frac{\tau}{B}\right). \tag{6}$$

Figure 5c shows the relative apparent time delay between two LFM pulses with opposite rates subjected to a common Doppler shift. By estimating the delay and inverting (6), it is possible to retrieve the Doppler shift affecting the received data. An accurate way to retrieve the Doppler shift is by computing the cross correlation between the data processed with a matched filter having positive rate and the same data processed with a matched filter having negative rate. The displacement of the peak of the cross correlation function

from half of the horizontal axis gives a measurement of the time delay between the up and down chirps. This concept is depicted in Figure 5d, where a shift of N samples (corresponding to a generic time delay) between the two LFM signals is reflected in a shift of N samples of the peak of the cross-correlation function. More details on the processing steps required to generate Doppler shift and backscattering products are given in Appendix A1.

3.5. Scientific Data Processing

The ocean winds processing takes the radiometrically calibrated backscatter product to derive winds near the ocean surface (at a nominal height of 10 m). Near-surface ocean wind vectors are derived from DopSCAT Level 1b data, by using a Geophysical Model Function (GMF), which relates σ° values to wind speed and direction. The wind retrieval is an inversion problem at each Wind Vector Cell (WVC) where, given a set of three σ° values (collected by the Fore, Aft, and Mid antennas) and the GMF, a set of ambiguous wind vectors is computed in a Bayesian optimization [*Portabella and Stoffelen*, 2006]. These 2–4 vectors have the highest probability of representing the true wind. Usually, two wind vectors are obtained as the most likely solutions, with directions separated by 180°. The measurement noise and the double harmonic nature of the GMF result in this dual wind direction ambiguity of two equal-probability solutions. Two GMFs are used in this work: the CMOD5n [*Verhoef et al*., 2008] and SSA2-CWM [*Fois et al*., 2015b]. A wind direction ambiguity removal step is further applied, based on a variational meteorological analysis and relying on prior numerical weather prediction (NWP) model wind and error information [*Vogelzang et al*., 2009]. The OVM retrieval is performed by searching for minimum distances between the Doppler measurements and the Doppler frequency corresponding to a certain OVM. To this aim, it is important to recall the relation between OVM and Doppler frequency, that is:

$$f_{D,i}^{OVM} = 2\frac{v_{OVM}}{\lambda}\sin(\theta_i)\cos(\phi_{AZ}^i), \tag{7}$$

where v_{OVM} is the OVM amplitude, θ_i is the incidence angle, and ϕ_{AZ}^i, $i \in (1,6)$, is the difference between the OVM direction and azimuth angle (i.e., 45°, 90°, 135° for Fore-Right, Mid-Right, and Aft-Right antennas, respectively). Note that the total sensitivity to OVM is somewhat dependent on incidence angle and azimuth with maximum OVM amplitude sensitivity in the outer swath for $\phi_{AZ}^{i=2,5} = 0^o \wedge 180^o$ and maximum OVM direction sensitivity for $\phi_{AZ}^{i=2,5} = 90^o \wedge 270^o$, resulting in a weakly nonlinear OVM retrieval. Maximum sensitivity corresponds to minimum error. The methodology adopted to extract the information relative to sea surface current relies on the hypothesis that at relatively low resolution (typically greater than 10 km by 10 km), the averaged interactions between current and wind are negligible in the measured ocean motion vector. Following this assumption, wind and currents effects can be considered as additive and a simple scheme to invert sea surface current vectors can be proposed, as suggested by equation (3). First, the wind field derived by DopSCAT is combined with NWP wind to remove directional ambiguities. The unambiguous wind vector is eventually used as input to CDOP or SSA2-CWM model to predict the sea state contribution to the geophysical OVM. Second, the residual OVM, which is expected to be related to the sea surface current, is derived by subtraction. As demonstrated by *Mouche et al*. [2012], NRCS and motion measurements can be combined in geographical areas free of strong currents to get better wind fields from the radar data. Following this approach, the existing algorithm to retrieve wind from ocean scatterometry could be adapted to get benefit of the motion information.

4. Performance Estimation

In this chapter, the performance of the proposed DopSCAT mission concept is assessed against the mission requirements presented in section 2. Level-1 performance is reported in Appendix A2. For Level-2 products, the performance is expressed against the scientific requirements. Finally, the end-to-end ability to produce simulated geophysical results from a synthetic scene is demonstrated to assess the expected performance of the mission. The oceanographic validation of DopSCAT surface currents is also elaborated.

4.1. End-to-End Simulator

The DopSCAT end-to-end simulator is a tool to simulate ad analyze the performance of the mission, i.e., from the observed scene to the retrieved Level-2 geophysical parameters. The architecture of the end-to-end simulator is schematically shown in Figure 6 and comprises different modules:

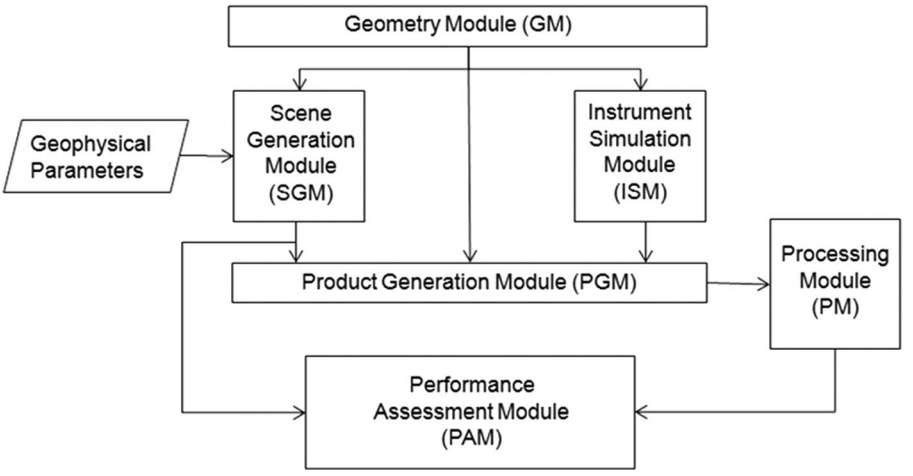

Figure 6. Block diagram of the DopSCAT End-to-End simulator.

4.1.1. Geophysical Parameters

The retrieval of OVWs is a nonlinear problem and the accuracy of the estimated winds depends on the wind input state. An average over different wind conditions is made to mitigate and possibly eliminate this dependence. The wind speed distribution is often represented by a Weibull distribution, with a maximum around 8 m/s, that is [*Lin et al.*, 2012].

$$f(v)=\frac{p2}{p1}\left(\frac{v}{p1}\right)^{p2-1}e^{-\left(\frac{v}{p1}\right)^{p2}} \tag{8}$$

where $p1 = 10$ m/s and $p2 = 2.2$ m/s.

4.1.2. Scene Generation Module

The GMFs are a empirically derived function that relate backscatter or wave motion measurements to surface wind vectors and viewing geometries (incidence angle, azimuth angle, wind vector). For C-band VV simulations, we use the CMOD5n or SSA2-CWM model for ocean backscatter and the SSA2-CWM or CDOP model for the wave motion.

4.1.3. Geometric Module

The correct determination of the ocean wind vector signature and the ocean vector motion, requires that every wind vector cell (WVC) on the surface be visited by three different views, corresponding to the views of the Fore, Mid, and Aft antennas. The observation geometry is calculated for every WVC in the swath using a simplified orbital model together with specific satellite pointing information.

4.1.4. Instrument Simulation Module

The backscatter variance depends on the instrument but also on the variability of the ocean surface (sub-WVC variability). For winds below 4 m/s, this variability is substantial. Moreover, the sub-WVC variability is sampled differently by the three beams, which have different SRFs, and this represents the largest contribution to the geophysical noise. The geophysical noise model is empirically modeled as a function of wind speed as: $k_g(v)=0.12\exp(-v/12)$ [*Portabella and Stoffelen*, 2006]. The instrumental and geophysical noise contributions are assumed Gaussian and uncorrelated.

4.1.4. Product Generation Module

The product generation module models the total scattering coefficient as:

$$\sigma^o=\sigma^o_{GMF}\left(1+\sqrt{k_p^2+k_g^2}\cdot N[0,1]\right) \tag{9}$$

This module expresses the total Doppler shift as:

$$f_D=(f_D^{GMF}+f_D^{Curr})\cdot \left(1+\sqrt{(\sigma^g_{f_D})^2+(\sigma^{X-corr}_{f_D})^2}\cdot N[0,1]\right) \tag{10}$$

where $N[0,1]$ is a Gaussian PDF with zero mean and unit standard deviation, $\sigma^{X-corr}_{f_D}$ is the uncertainty related to the cross-correlation operation, and $\sigma^g_{f_D}$ is the uncertainty in Doppler related to the geophysical

noise. The modeling of the geophysical error is very complicated. In principle, such a model should take into account for all those effects and dependences that are not considered in the GMF. As an example, imperfections of the geophysical model function, rain, atmospheric, and wave-field variability can affect the accuracy of both backscatter and Doppler measurements. However, thanks to the coarse spatial resolution of the scatterometer, these effects have a very little impact on the accuracy of wind vector retrieval, with some exceptions represented by confused sea state, high wind variability, and intense rain. These special cases occur less than 5% of time in a year. In these cases, the quality of the retrieved winds and Doppler shift is seriously compromised.

4.1.6. Processing Module

The retrieval of ocean winds from scatterometer data relies on the use of GMFs, which relate the state variables, i.e., wind speed and wind direction, to backscatter measurements. The Bayesian wind inversion is based on a search for minimum distances between backscatter measurements and backscatter model solutions lying on the empirical GMF surface [*Portabella and Stoffelen*, 2006]. We define the normalized square distance MLE($\mathbf{v}|\mathbf{z}$) from backscatter observations $z = (\sigma^{\circ})^{0.625}$ to backscatter wind solutions $z_{GMF}(\mathbf{v})$ on the GMF surface as:

$$MLE(\mathbf{v}|z) = \frac{1}{\langle MLE \rangle} \sum_{i=1\ldots N} |z_i - z_{GMF,i}(\mathbf{v})|^2 \tag{11}$$

where N is the dimension of the backscatter vector (i.e., the number of views per WVC), and $<MLE>$ is an empirical normalization factor that accounts for the instrumental noise variance, var{σ°}, and deviations from the ocean wind GMF due to geophysical noise. It is worth noting that, three azimuth views (from the fore, aft and mid antennas) are needed to retrieve unambiguously the wind vector and this is a fundamental input for the surface current retrieval. Once the wind retrieval has been completed, the OVM retrieval step is started:

$$MLE(\mathbf{v}_{OVM}|f_D) = \sum_{i=1\ldots N} |f_{D,i} - \hat{f}_{D,i}(\mathbf{v}_{OVM})|^2. \tag{12}$$

The OVM is retrieved by searching for minimum distances between the Doppler measurements and the Doppler frequency corresponding to a certain OVM (see equation (7)), finally resulting in a OVM vector. Subsequently, the SSA2-CWM (or CDOP) GMF is used to estimate the local sea state OVM contribution. By subtracting the sea state motion vector from the total geophysical motion vector, we can derive potential ocean currents, as per equation (3).

4.2. Level-2 Performance

The estimation of the performance of Level-2 product retrievals has been performed on the basis of simulated and real data from ASCAT [*Gelsthorpe et al.*, 2000] wind fields and from OSCAR [*Johnson et al.*, 2007] ocean current fields. The wind vector data by ASCAT together with the observation geometry are used as input to the geophysical model functions (e.g., SSA2-CWM, CMOD5n, CDOP) to generate backscatter maps and wind-driven Doppler-frequency maps. Ocean current vector measured by OSCAR are, instead, used together with the geometry of observation to compute the Doppler shift associated to the current. All these operations are performed by the scene generation module (SGM). The instrument generation module, instead, computes the Signal-to-Noise Ratio (SNR) and the Radiometric Resolution (k_p) starting from geometrical information and σ^0 maps (see equation (1)). The product generation module PGM, corrupts the σ^0 and the Doppler frequency simulated data by adding instrumental, geophysical, and processing errors, as per equations (9) and (10). The Level-2 processor takes the corrupted data of the PGM as inputs and, by applying equation (11), it first derives the wind vector and then uses the wind vector to compute the wind-driven frequency shift. This quantity is subtracted from the measured Doppler shift (computed via cross-correlation between up and down chirp) to obtain sea surface current vectors. Equation (12) is finally used to retrieve potential surface currents. Simulations with DopSCAT end-to-end simulator indicate that the accuracy objectives of 0.1 m/s specified for the current product are close to being achieved over a wide range of wind speed and directions. Performance analysis of Level-2 data product has been carried out considering all possible system sources of errors (e.g., instrument and geophysical noise). Figure 7a and 7b show an example of ASCAT wind field used in the simulation: both wind speeds and directions are depicted (only the right swath is shown). Horizontal and vertical axis show the geographic longitude and the latitude

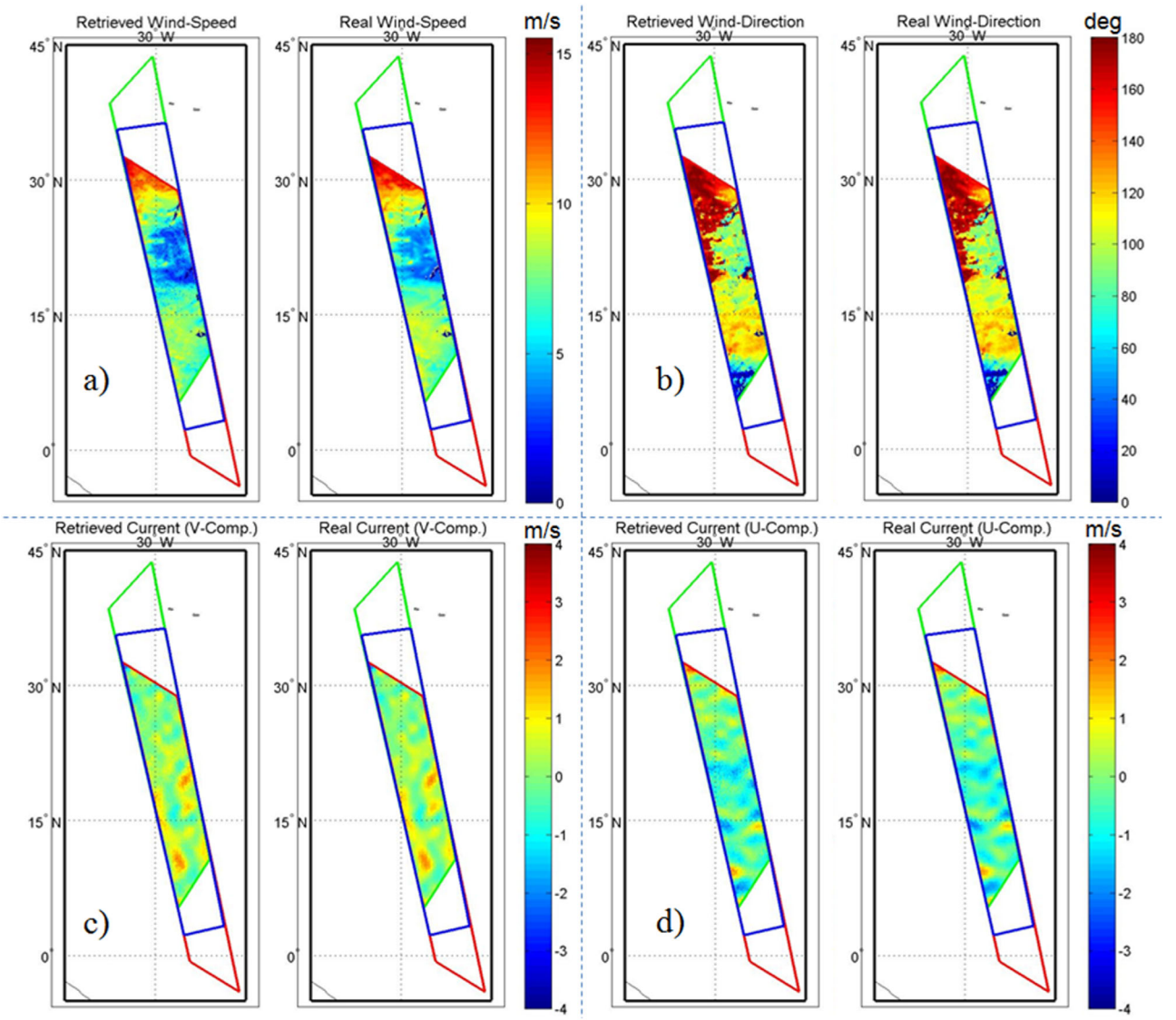

Figure 7. (a) and (b) Comparison between real and retrieved wind vectors (VV-pol case); (c) and (d) Comparison between real and retrieved sea surface current vectors. Green, blue, and red polygons represent the fore, mid, and aft swaths. The interception between the three areas identifies those data where the retrieval can be applied.

of the observed area. In the same figures, three different polygons are illustrated: they correspond to the swaths illuminated by the three right antennas of DopSCAT. In particular, the green polygon refers to the fore antenna, the red to the aft antenna, and the blue one to the mid antenna. Only the data within the common area are used in the Level-2 processing. Figures 7a and 7b show the result of the wind retrieval by using (11) on VV-pol data. As also shown in Figures 8a and 8b, the accuracy in wind speed is better than 0.7 m/s, whereas the accuracy in wind direction is better than 7 degrees. Figure 8 shows the two-dimensional histograms of the retrieved wind solution versus the real wind for wind speed (Figure 8a) and wind direction (Figure 8b). Note that the right plot is computed for winds larger than 4 m/s. This is done to avoid the noise produced by the typical low wind direction skill at low winds (i.e., the wind direction error increases with decreasing wind speed). With reference to the same Figure 8, *N* is the number of data; mx and my are the mean values along the x and y axis, respectively; m(y−x) and s(y−x) are the bias and the standard deviation with respect to the diagonal, respectively; and cor_xy is the correlation value between the x and y-axis distributions. The contour lines are in logarithmic scale: 10 contour levels are plotted. Results of the retrieval are shown in Figure 7c and 7d for both horizontal components of the ocean current. Figures 8c and 8d provide the two-dimensional histograms of the retrieved components of current versus the real components of current. The figures show almost no bias in current speed and very small standard

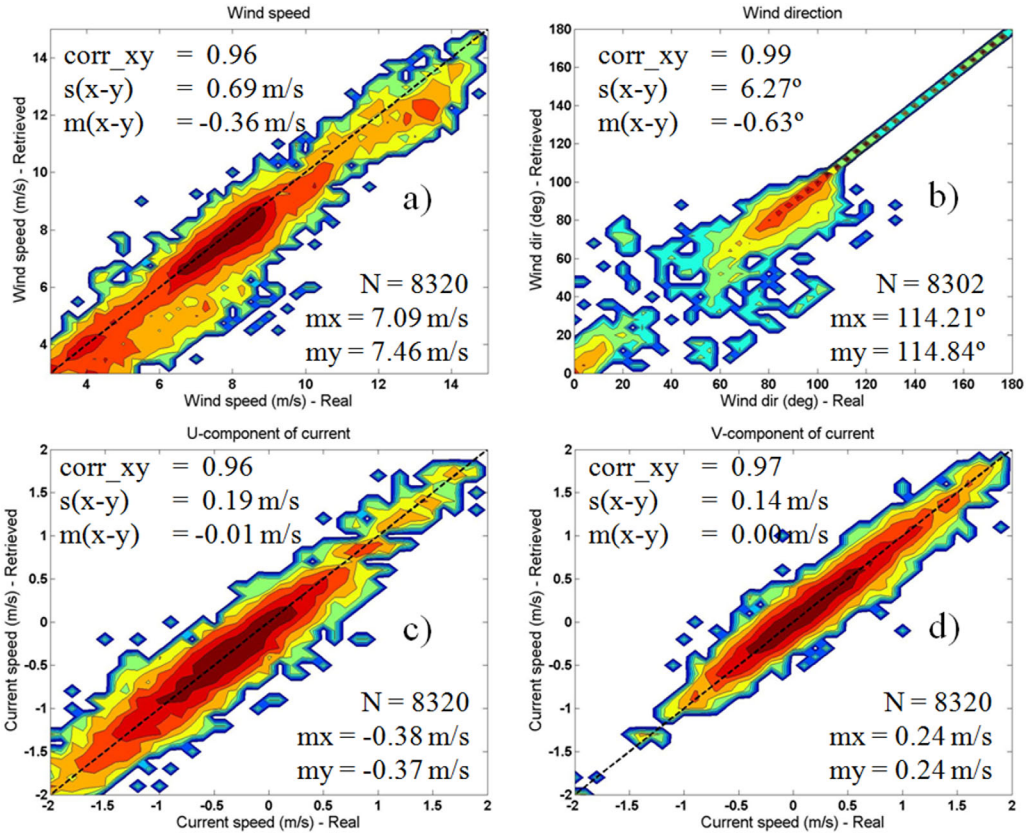

Figure 8. (a) Two-dimensional histogram of the retrieved wind speed versus the real wind speed; (b) two-dimensional histogram of the retrieved wind direction versus the real wind direction (only winds above 4 m/s are used in the wind direction plot); (c) two-dimensional histogram of the retrieved zonal component of the ocean current vector versus the real zonal component of the ocean current vector; (d) same as Figure 8c but for the meridional component of the ocean current vector.

deviations (i.e., 0.14 m/s and 0.19 m/s for the meridional and zonal component, respectively). Extensive Monte-Carlo simulations over several possible wind and current scenarios have demonstrated the capability of the present DopSCAT concept in estimating ocean currents with accuracy below 0.2 m/s, at a spatial resolution of 25 km (i.e., spatial sampling of 12.5 km) and a temporal resolution of 24 h. With reference to the user requirements in Table 1, a spatial resolution of 25 km is not sufficient to cover coastal applications (such as search and rescue, marine renewable energy, oil and gas) but it would be more than adequate for most of the applications. The higher resolution product can, on one hand, extend the use of DopSCAT to coastal areas but, on the other hand, the accuracy of the estimated currents would be degraded. In fact, the accuracy depends on the radiometric resolution, which in turn depends on the number of looks and thus on the spatial resolution of the product. For high-resolution products, we expect an accuracy worse than 1 m/s in the ocean current estimates, which is only sufficient to meet the users' needs by performing temporal averages on, e.g., a monthly time scale.

4.3. Oceanographic Validation of DopSCAT Surface Currents

In order to validate the method proposed to map the geophysical Doppler shifts into a sea surface current information, references for sea surface current measurements are needed. In situ measurements are good candidates to get reliable and direct sea surface measurements. Surface drifters are routinely dropped in the ocean and data base of these measurements are accessible. They provide ocean current measurement at a 15 m depth. Colocation of DopSCAT measurements with drifters will enable to compare observed sea surface current with in situ data. A similar approach was used for ENVISAT's ASAR WS data to show the ability of the SAR to quantitatively measure sea surface currents [*Chapron et al.*, 2005]. Other in situ measurements could be used. In particular with Argos buoys (http://argo.ucsd.edu), it is possible to get the sea surface current. The ocean surface currents over the globe are of many kinds. Various time and space scales

as well as intensities of speed coexist and it would be unrealistic to present DopSCAT as the ultimate solution for the study of all the types of currents. Ocean Doppler scatterometers could be used for daily global mapping to cover scales between 20 and 100 km. This range scale constraints the selection of suitable regions for validation. In particular, narrow coastal currents, ocean fronts, or tidal currents should be discarded. A number of regions can be suitable for the validation of DopSCAT ocean current products. Among the Equatorial currents, we suggest the Equatorial Pacific current. This area is very well equipped with Tropical Atmosphere Ocean (TAO) buoys (http://www.pmel.noaa.gov/tao/) and it has already been used to observe the signature of the currents in scatterometers data [*Kathryn et al*., 2005]. In particular, comparisons between TAO anemometer and QuikSCAT scatterometer winds were analyzed (over a period of 3 years) and systematic differences in winds were observed. Monthly averaged collocated wind differences (CWDs) were compared with available near-surface current data at 15 m depth from drifters, at 25 m depth from acoustic Doppler current profilers (ADCPs), and at 10 m depth from current meters and with geostrophic currents at the surface from the TOPEX/Poseidon radar altimeter, showing very good agreement.

Among the western boundary currents, the Agulhas and the Gulf stream are probably the most adequate sites. They are characterized by large, steady, and intense flows which should induce a strong signature in the Doppler signal. Regions where these two currents occur with the largest intensity are known and huge SAR data sets exist. Moreover, these regions are well covered by Drifters which could also be used for validation. A validation area such as the Gulf stream is also of interest because of the generation of ocean mesoscale eddies. Their length scale of typically 20–50 km are consistent with the DopSCAT resolution. The massive deployment of drifting buoys and colocated high-resolution high-frequency radar data by the NOAA's Integrated Ocean Observing System (IOOS) makes this area suitable for frequent ocean current calibration. The IOOS office maintain more than 130 individual radars, all contributing data to a national network that provides estimates of surface currents over much of the coastal areas in U.S. This network provides surface velocities and predictions of particle trajectories for a wide range of scientific and operational uses. HF radar sites obtain radial resolutions of 2–8 km out to ranges of approximately 45–130 km, depending on the operating frequency. These radars can provide surface velocities with accuracies in the order of a few centimeters per second. Comparisons between DopSCAT and HF radars data can be made by averaging the measured surface velocities over the resolution cell of the Doppler scatterometer. In order to verify whether the observed DopSCAT surface currents are of real nature, the use of colocated Sea Surface Temperature (SST) data from MetOp Advance Very High Resolution Radiometer (AVHRR) and Infrared Atmospheric Sounder Interferometer (IASI) would be of paramount importance, as SST gradients and fronts are typically linked to ocean currents. The AVHRR provides global imagery twice a day at 1 km spatial resolution (at nadir), in the visible and infrared bands of the electromagnetic spectrum. The IASI instrument measures the infrared part of the electromagnetic spectrum at horizontal resolution of 12 km over a swath width of about 2200 km. Thermal and visible imagery represents an alternative viable way of estimating advective ocean surface currents from sequential infrared satellite imagery, by means of the Maximum Cross-Correlation (MCC) technique [*Emery et al*., 1986; *Crocker et al*., 2007]. This technique has been proven to be useful in mapping the short space and time scale structures of the East Australian Current [*Bowen et al*., 2002, 2005], the California Current [*Tokmakian et al*., 1990], the Gulf Stream, and the coastal waters off British Columbia [*Emery et al*., 1986, 1992]. Over areas that show strong and coherent features over several days (e.g., the Gulf Stream), the MCC method technique could be a powerful tool to validate the DopSCAT ocean current products. An instrument like IASI, if loaded on board the same satellite, would be able to fill the nadir gap left by DopSCAT ocean current product between -20° and $+20^\circ$ incidence (see Figure 4). *Kudryavtsev et al*. [2012a, 2012b] have developed a method to retrieve and interpret fine spatial variations of the sea surface roughness in sun glitter optical imagery. The retrieval processing makes use of a transfer function relating the sun glitter brightness contrast to the mean square slope contrast. The results document significant benefit from the synergetic use of sun glitter and radar imagery for quantitative investigations of surface signatures of ocean phenomena, including internal waves and mesoscale ocean currents. Spatial variations of the sea surface roughness are correlated with sea surface temperature gradients. The approach proposed by *Kudryavtsev et al*. [2012a, 2012b] of combining SST, sun glitter brightness (provided, for example, by DLR METimage instrument onboard MetOp-second Generation) and radar backscatter anomalies, augmented possibly by other satellite data (e.g., scatterometers, altimetry, ocean color), can provide consistent and quantitative determination of the location and intensity of surface currents that could be used to validate the DopSCAT current products. Another MetOp instrument that could be used in synergy with DopSCAT, for the purpose of its product validation, is the MicroWave

Imager (MWI). The MicroWave Imager can be used to derive sea-ice motion by following the displacement of brightness temperature features in sequential images [*Kimura and Wakatsuchi*, 2000]. The procedure for the calculation of ice motion is based on the maximum cross-correlation method [*Ninnis et al*., 1986; *Emery et al*., 1991]. By using the *Thorndike* and *Colony* [1982] relationship between the ice motion and geostrophic wind, the mean ocean current can be derived. In particular, the sea-level pressure data produced by the European Centre for Medium-Range Weather Forecasts (ECMWF) can be used for the calculation of the geostrophic wind. The effect of the geostrophic wind can eventually be subtracted from the ice motion to generate ocean surface current maps.

5. Conclusions and Recommendations

Ocean Doppler scatterometry can provide simultaneous and accurate measurements of wind fields and ocean motion vectors that can be used to generate global surface ocean current maps at a spatial resolution of 25 km (i.e., 12.5 km spatial sampling) on a daily basis (thanks to the very large swath). These maps will allow gaining some insights on the upper ocean mesoscale dynamics. From the user product requirements and measurement system requirements, an innovative instrument concept, named DopSCAT, is derived. Special focus is given to the observation principle, the scientific data processing, and the validation of the resulting sea surface products. An end-to-end performance estimation of the DopSCAT mission is carried out using simulated input data sets that are generated either from ASCAT and OSCAR data or from the simulator itself by using values inferred from real data.

Results of nominal Level 2 product simulations indicate that the threshold requirement of 0.2 m/s accuracy in sea surface current will be met for a wide range of conditions. It is particularly important to note that the goal requirement of 0.1 m/s is very close to being met apart for cases of low wind speeds ($<$5 m/s) at far swath locations. The analysis of high-resolution products indicates a higher RMSE ($>$1 m/s), which is currently not compliant with the 0.2 m/s threshold requirement. Nevertheless, the resolution of the nominal product would allow covering most of the users' applications listed in Table 1.

The DopSCAT concept represents a major improvement with respect to current and future planned wind-scatterometers, as it provides the unique capability of simultaneous measurements of Ocean Vector Wind and Ocean Vector Motion on a global scale, together with the capability of measuring very strong wind speeds (up to 60 m/s) through the use of cross-polarization. At instrument level, no critical elements have been identified for the DopSCAT development. The DopSCAT subsystems are, in fact, entirely based on heritage from past and current C-band radar missions (e.g., MetOp's ASCAT, MetOp-SG's SCA, Sentinel-1, RADARSAT-2).

Appendix A

A1. Level-1 Data Processing and Performance

In this appendix, an overview of the processing steps going from the Level-0 products to the Level-1 products is given. The whole processing flow is depicted in Figure A1 and consists of two main chains for the generation of σ° images (Figure A1a) and Doppler shift measurements (Figure A1b). The generation of σ° measurements foresees the following main basic processing steps.

Doppler Centroid Compensation (DC): this block performs the Doppler Centroid compensation starting from motion and geometric information provided by the platform Attitude and Orbit Control Systems (AOCS) and then compensated across the image. After this processing step, the Doppler spectrum is sitting in baseband. The predicted geometrical Doppler shift is given by the relative velocity of the satellite and the rotating Earth according to a general formula demonstrated by *Raney* [1986]. The DC estimate will be further refined by measuring the Doppler shift over land areas.

Separation Compression Filter (SCF): this block is used to separate the dual chirp echo signal into an up chirp component and a down chirp component, thus avoiding undesired interferences from down chirps to up chirps and vice versa. The SCF procedure has to be performed after geometrical DC compensation in order to be effective [*Tagawa et al*., 2004].

Range Compression: this block performs a convolution along the range direction between the raw data and the chirp replica.

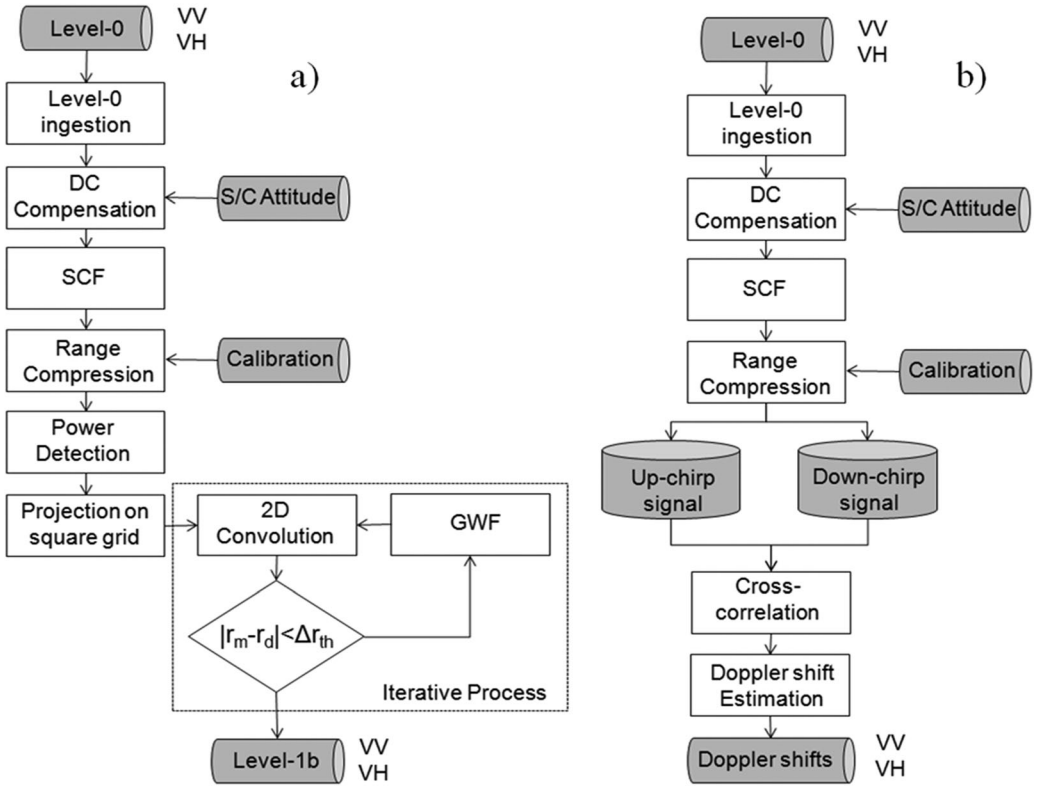

Figure A1. Level-1 data processing flow for the generation of Normalized Radar Cross section images (left) and for the estimation ocean's Doppler shifts (right).

Projection on a Square Grid: this step consists of a projection of the range-compressed data on a regular grid of Wind Vector Cells (WVC). The spacing of the measurement WVCs in along and across-track directions represents the spatial sampling of the product (i.e., 12.5 km for the nominal product and 6.25 km for the high-resolution product).

Convolution with Ground Weighting Function: after power detection and slant-to-ground projection of the image, we perform an aggregation of the detected compressed signals in a box centered in the WVC for each beam and polarization [*Verhoef et al*., 2012], that is

$$GWF(x,y)=w\left(\frac{x}{L_x},\frac{y}{L_y}\right), \tag{A1}$$

with L_x, L_y being respectively the across and along-track dimensions of the GWF. This convolution is performed at each WVC and operates a spatial aggregation, per beam, in along and across-track directions. The main objective of this averaging is to obtain a set of σ° measurements (one per beam) for each WVC in each swath at the desired spatial resolution and radiometric resolution. The results of these convolutions are called Spatial Response Functions (SRFs). As depicted in Figure A1b, the generation of the Doppler shift products requires the range-compression with both up and down chirp reference functions. In this way, two different range-compressed images are obtained. A cross correlation of the two images is then performed. The Doppler shift is given by the location of the maximum of the cross-correlation function. The accuracy of the time shift (t_s) estimates is given by the Cramèr-Rao lower bound [*Quazi*, 1981]:

$$\sigma_{t_s}^2 \geq \left\{2T\int_{f_1}^{f_2}(2\pi f)^2\frac{|\gamma(f)|^2}{1-|\gamma(f)|^2}df\right\}^{-1}, \tag{A2}$$

where $\gamma(f)$ is the coherence function, which is defined as $|\gamma(f)|^2=S(f)^2/[S(f)+N(f)]^2$, where $S(f)$ and $N(f)$ are the signal and noise autospectra. The parameter $T=2r\sin\theta_i/c$ is the observation time (that depends on the resolution, r, of the Doppler estimates) and $B=f_2-f_1$ is the bandwidth. The cross correlation is

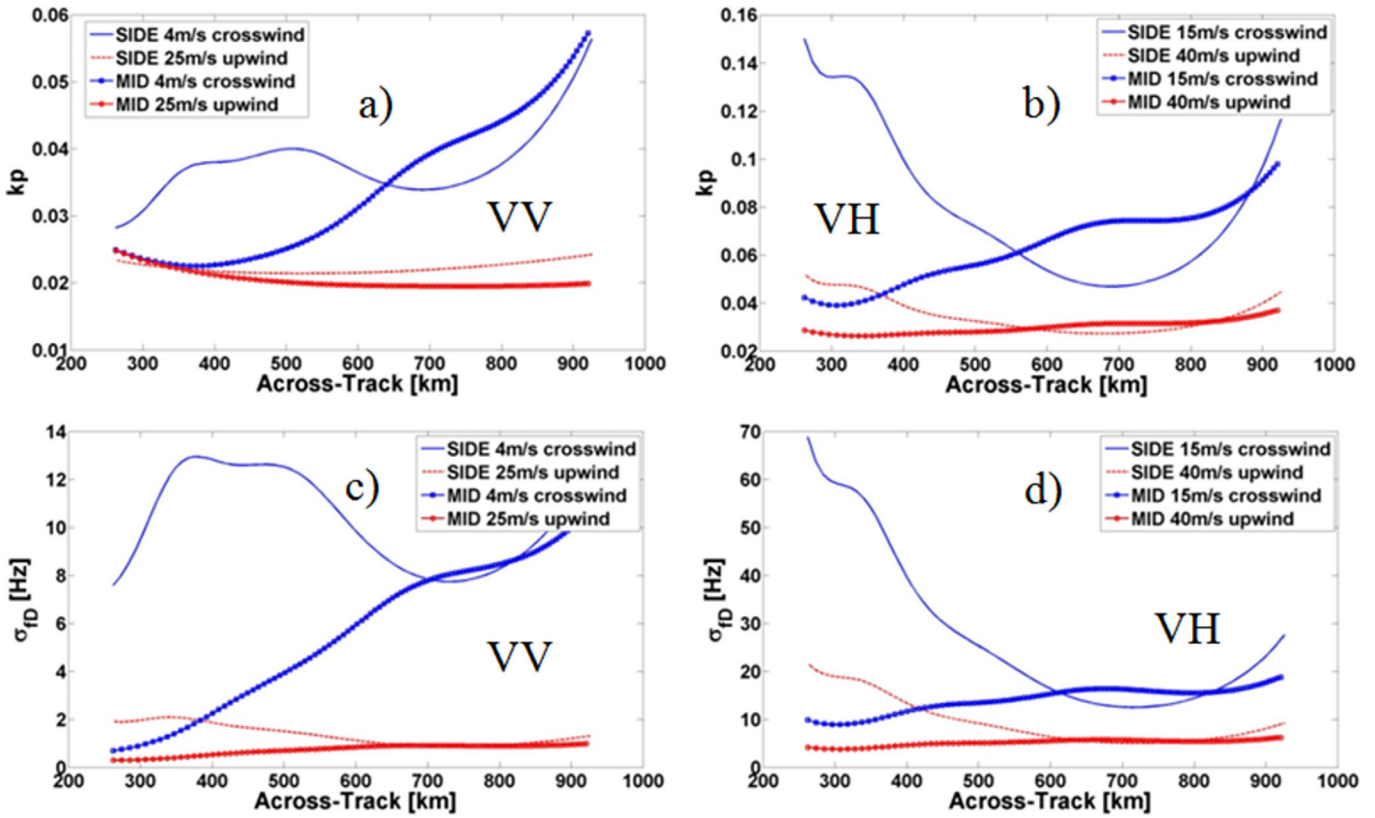

Figure A2. (a) radiometric resolution in VV-polarization versus across-track position for both mid and side swaths in the two extreme wind cases, i.e., 4 m/s cross-wind and 25 m/s upwind; (b) radiometric resolution in VH-polarization versus across-track position for both mid and side swaths in the two extreme wind cases, i.e., 15 m/s cross-wind and 40 m/s upwind; (c) and (d) accuracy in the estimation of the Doppler shift for VV and VH-polarizations.

performed within a window of duration T sliding across the entire swath (from near swath to far swath). The accuracy of the Doppler shift estimates, corresponding to t_s, can be obtained as:

$$\sigma_{f_D} = \sigma_{t_s}\left(\frac{B}{\tau}\right). \quad \text{(A3)}$$

After the computation of the cross correlation, some oversampling (by zero padding) might be needed to improve the precision in the estimation of f_D. In the same Wind Vector Cell (WVC), we might be able to collect several (N_{obs}) Doppler measurements (one per Tx-pulse). The higher the Pulse Repetition Frequency of the DopSCAT instrument, the higher N_{obs}. We can use these N_{obs} measurements to improve the accuracy of the Doppler estimates.

Table 2. DopSCAT Parameters

Parameters	UoM	Value
Orbital semimajor axis	(km)	7195,605347
Orbital eccentricity	(#)	0,001165
Orbital inclination	(°)	98,702198
RAAN	(°)	62,4731
Argument of perigee	(°)	90
Peak power	(W)	2200 (1.1 kw per TWT)
Carrier frequency	(GHz)	5,3
Pulse duration	(ms)	2
Tx signal	(#)	Double chirp
ChirpRate (MID-ANT)	(kHz/ms)	417,5
ChirpRate (SIDE-ANT)	(kHz/ms)	205
PRF	(Hz)	32
Tx+Rx front-end Losses	(dB)	3,4
Noise figure	(dB)	1,4
MID-ANT length	(m)	2,87
MID-ANT height	(m)	0,32
SIDE-ANT length	(m)	3,21
SIDE-ANT height	(m)	0.32
Spatial resolution	(km × km)	25 × 25
Spatial sampling	(km × km)	12,5 × 12,5
Number of antennas	(#)	6
Polarization [MID-ANT]	(#)	VV and VH (for high wind)
Polarization [SIDE-ANT]	(#)	VV and VH (for high wind)
Swath size	(km)	2 × 660
Min. incidence angle	(°)	20

A2. Level-1 Performance

Table 2 provides a complete list of DopSCAT parameters and information used for the assessment of its Level-1 performance. The radiometric performance achieved by the DopSCAT instrument is largely a function of the radiation pattern generated by the antenna subsystem.

Both side and mid antenna patterns are optimized for a performance swath limited by a minimum incidence angle of 20° and a maximum incidence angle of 65°. The variations in the radiometric resolution and total ambiguity ratio as a function of the incidence angle are shown in Figures A2a and A2b. The VH-polarization represents the worst-case scenario for *kp*. This depends entirely on the ocean backscattering, which is lower in VH than in VV polarization. The curves correspond to the lowest altitude (823 km) over the orbit, however no significant differences are found at the highest altitude (849 km). Radiometric resolution performance show sufficient margins with respect to the requirements reported in section 2. Figures A2c and A2d provide the accuracy in the estimation of the Doppler shift for VV and VH-polarization, respectively.

Acknowledgments

The present work was funded by RHEA System S.A. and motivated by ESA's General Study Programme, "Feasibility Investigation of Global Ocean Surface Current Mapping using ERS, MetOp and QuikScat Wind Scatterometer," AO/1-6303/09/NL/AF. The authors wish to thank Paul Hwang Paul Hwang, NRL, for the provision of the wave height spectrum used in Figures 1, 2, and 3. Tania Casal and Craig Donlon, ESA/ESTEC, deserve a special thank, for the support in the definition of the DopSCAT objectives and user requirements. The authors thank also Pierre Fabry, Along-Track, and Andrea Recchia, Aresys, for the interesting discussions on DopSCAT principle of observation and data processing. The authors would like to acknowledge the two anonymous reviewers and John Matthews, Kyoto University, for their invaluable advises which significantly improved the manuscript. The ASCAT data in BUFR and NetCDF format were ordered online from the EUMETSAT Data Centre: http://www.eumetsat.int/website/home/Data/DataDelivery/EUMETSATDataCentre/index.html. OSCAR data were available from: ftp://podaac-ftp.jpl.nasa.gov/allData/oscar/preview/L4/oscar_third_deg. Both Envisat-ASAR and Sentinel-1 clouds of NRCS measurements (used in Figures 2 and 3), were provided by the Institut Français de Recherche pour l'Exploitation de la Mer (IFREMER).

References

Abdalla, S. (2014), Calibration of SARAL/AltiKa wind speed, *IEEE Geosci. Remote Sens. Lett.*, *11*(6), 1121–1123.

Bannoura, W. J., A. Wade, and D. N. Srinivas (2005), NOAA Ocean Surface Topography Mission Jason-2 project overview in OCEANS, *Proceedings of MTS/IEEE*, vol. 3, pp. 2155–2159, doi:10.1109/OCEANS.2005.1640083.

Bowen, M. M., W. J. Emery, J. Wilken, P. C. Tildesley, I. J. Barton, and R. Knewtson, (2002), Extracting multi-year surface currents from sequential thermal imagery using the maximum cross correlation technique, *J. Atmos. Oceanic Technol.*, *19*(10), 1665–1676.

Bowen, M. M., J. L. Wilkin, and W. J. Emery, (2005), Variability and forcing of the East Australian current, *J. Geophys. Res.*, *110*, C03019, *doi*: 10.1029/2004JC002533.

Chapron, B., F. Collard, and F. Ardhuin (2003), Satellite SAR Sea surface Doppler measurements, in *Proceedings of 2nd Workshop on Coastal and Marine Application of SAR*, 8–12 Sept., Svalbard, Norway, *Eur. Space Agency Spec. Publ.*, *ESA-SP565*, pp. 133–139.

Chapron, B., F. Collard, and F. Ardhuin (2005), Direct measurements of ocean surface velocity from space: Interpretation and validation, *J. Geophys. Res.*, *110*, C07008, *doi*:10.1029/2004JC002809.

Crocker, R., D. K. Matthews, W. J. Emery, and D. G. Baldwin (2007), Computing coastal ocean surface currents from infrared and ocean color satellite imagery, *IEEE Trans. Geosci. Remote Sens.*, *45*(2), 435–447.

Donlon C. (2013), ESA Data User Element (DUE) GlobCurrent User Requirement Document (URD), *ESA Rep. EOP-SM/2451/CD-cd*, European Space Agency, Technical Report. [Available at http://web.nersc.no/globcurrent/.]

Durand, M., F. Lee-Lueng, D. P. Lettenmaier, D. E. Alsdorf, E. Rodriguez, and D. Esteban-Fernandez, (2010), The surface water and ocean topography mission: Observing terrestrial surface water and oceanic submesoscale eddies, *IEEE Proc.*, *98*(5), 766–779.

Elfouhaily, T., B. Chapron, K. Katsaros and D. Vandemark (1997), A unified directional spectrum for long and short wind-driven waves, *J. Geophys. Res.*,*102*, 15,781–15,796.

Emery, W. J., A. C. Thomas, M. J. Collins, W. R. Crawford, and D. L. Mackas (1986), An objective method for computing advective surface velocities from sequential infrared satellite images, *J. Geophys. Res.*, *91*, 12,865–12,878.

Emery, W. J., C. W. Fowler, J. Hawkins, and R. H. Preller (1991), Fram Strait satellite image-derived ice motions, *J. Geophys. Res.*, *96*, 4751–4768.

Emery, W. J., C. Fowler, and A. Clayson, (1992), Satellite-image-derived Gulf Stream currents compared with numerical model results, *J. Atmos. Oceanic Technol.*, *9*(3), 286–304.

Fabry, P., et al. (2013), Feasibility study of sea surface currents measurements with Doppler scatterometers, in *ESA Living Planet Programme*, Eur. Space Agency, Edinburgh, U. K.

Fernandez, D. E., J. R. Carswell, S. Frasier, P. S. Chang, P. G. Black, and F. D. Marks (2006), Dual-polarized C- and Ku-band ocean backscatter response to hurricane-force winds, *J. Geophys. Res.*, *111*, C08013, doi:10.1029/2005JC003048.

Fois, F., P. Hoogeboom, F. Le Chevalier, and A. Stoffelen (2014), Future ocean scatterometry at very strong winds, in *IEEE International Geoscience and Remote Sensing Symposium (IGARSS)*, pp. 3886–3889, IEEE, 13–18 July, doi:10.1109/IGARSS.2014.6947333.

Fois, F., P. Hoogeboom, F. Le Chevalier, and A. Stoffelen (2015a), Future ocean scatterometry: On the use of cross-polar scattering to observe very high winds, *IEEE Trans. Geosci. Remote Sens.*, *53*(9), 5009–5020 doi:10.1109/TGRS.2015.2416203.

Fois, F., P. Hoogeboom, F. L. Chevalier, and A. Stoffelen (2015b), An analytical model for the description of the full-polarimetric sea surface Doppler signature, *J. Geophys. Res. Oceans*, *120*, 988–1015, doi:10.1002/2014JC010589.

Fu, L.-L., D. B. Chelton, P.-Y. Le Traon, and R. Morrow. (2010), Eddy dynamics from satellite altimetry, *Oceanography*, *23*(4):14–25, doi: 10.5670/oceanog.2010.02.

Galin, N., D. J. Wingham, R. Cullen, M. Fornari, W. H. F. Smith, and S. Abdalla (2013), Calibration of the CryoSat-2 Interferometer and Measurement of Across-Track Ocean Slope, *IEEE Trans. Geosci. Remote Sens.*, *51*(1), 57–72.

Gelsthorpe, R. V., E. Schied, and J. J. W. Wilson (2000), ASCAT-Metop's advanced scatterometer, *ESA Bull. 102*, 19–27.

Gommenginger, C., B. Chapron, J. Marquez, B. Richards, M. Caparrini, G. Burbidge, D. Cotton, and A. C. H. Martin (2014), Wavemill: A new mission for high-resolution mapping of total ocean surface current vectors, in *Proceedings of* EUSAR 2014; 10th *European Conference on Synthetic Aperture Radar*; pp. 1–4.

Hasselmann, K. (1962), On the nonlinear energy transfer in a gravity-wave spectrum. Part 1: General theory, *J. Fluid Mech.*, *12*, 481–500.

Hwang, P. A., D. M. Burrage, D. W. Wang, and J. C. Wesson, (2013), Ocean surface roughness spectrum in high wind condition for microwave backscatter and emission computations, *J. Atmos. Oceanic Technol.*, *30*, 2168–2188.

Hwang, P. A. and F. Fois, (2015), Surface roughness and breaking wave properties retrieved from polarimetric microwave radar backscattering, *J. Geophys. Res. Oceans*, *120*, 3640–3657, doi:10.1002/2015JC010782.

Hwang, P. A., B. Zhang, and W. Perrie (2010a), Depolarized radar return for breaking wave measurements and hurricane wind retrieval, *Geophys. Res. Lett.*, *37*, L01604, doi:10.1029/2009GL041780.

Hwang, P. A., B. Zhang, J. V. Toporkov, and W. Perrie (2010b), Comparison of composite Bragg theory and quad-polarization radar backscatter from RADARSAT-2: With applications to wave breaking and high wind retrieval, *J. Geophys. Res.*, *115*, C08019, doi:10.1029/2009JC005995.

Hwang, P. A., W. Perrie, and B. Zhang (2014), Cross-polarization radar backscattering from the ocean surface and its dependence on wind velocity, *IEEE Geosci. Remote Sens. Lett.*, *11*(12), 2188–2192.

Johannessen, J. A., B. Chapron, F. Collard, V. Kudryavtsev, A. Mouche, D. Akimov and K.-F. Dagestad (2008), Direct ocean surface velocity measurements from space: Improved quantitative interpretation of Envisat ASAR observations, *Geophys. Res. Lett.*, *35*, L22608, doi: 10.1029/2008GL035709.

Johnson, E. S., F. Bonjean, G. S. E. Lagerloef, J. T. Gunn, and G. T. Mitchum, (2007), Validation and error analysis of OSCAR sea surface currents, *J. Atmos. Oceanic Technol.*, *24*, 688–701, doi:10.1175/JTECH1971.1.

Kelly, K. A., S. Dickinson, and G. C. Johnson, (2005), Comparisons of scatterometer and TAO winds reveal time-varying surface currents for the tropical pacific ocean, *J. Atmos. Oceanic Technol.*, *22*, 735–745, doi:10.1175/JTECH1738.1.

Kimura N., and M. Wakatsuchi (2000), Relationship between sea-ice motion and geostrophic wind in the northern hemisphere, *Geophys. Res. Lett.*, *27*, 3735–3738.

Kudryavtsev, V., A. Myasoedov, B. Chapron, J. A. Johannessen, and F. Collard (2012a), Joint sun-glitter and radar imagery of surface slicks, *Remote Sens. Environ.*, *120*, 123–132. [Available at http:10.1016/j.rse.2011.06.029.]

Kudryavtsev, V., A. Myasoedov, B. Chapron, J. A. Johannessen, and F. Collard (2012b), Imaging mesoscale upper ocean dynamics using synthetic aperture radar and optical data, *J. Geophys. Res.*, *117*, C04029, doi:10.1029/2011JC007492.

Le Roy, Y., M. Deschaux-Beaume, C. Mavrocordatos, and F. Borde (2009), SRAL, a radar altimeter designed to measure a wide range of surface types, in *IEEE International, IGARSS 2009, Geoscience and Remote Sensing Symposium*, vol. 5, pp. V-445–V-448, IEEE, 12–17 July, doi:10.1109/IGARSS.2009.5417636.

Lin, C. C., M. Betto, M. B. Rivas, A. Stoffelen, and J. de Kloe (2012), EPS-SG wind scatterometer concept tradeoffs and wind retrieval performance assessment, *IEEE Trans. Geosci. Remote Sens.*, *50*(7), 2458–2472, doi:10.1109/TGRS.2011.2180393.

Longuet-Higgins, M. S. (1963), The effect of nonlinearities on statistical distributions in the theory of sea waves, *J. Fluid Mech.*, *17*(3), 459–480.

Mouche, A., and B. Chapron (2015), Global C-Band Envisat, RADARSAT-2 and Sentinel-1 SAR measurements in copolarization and cross-polarization, *J. Geophys. Res. Oceans*, *120*, doi:10.1002/2015JC011149.

Mouche, A. A., B. Chapron, N. Reul, and F. Collard (2008), Predicted Doppler shifts induced by ocean surface wave displacements using asymptotic electromagnetic wave scattering theories, *Waves Random Complex Media*, *18*(1), 185–196.

Mouche, A. A., F. Collard, B. Chapron, K. Dagestad, G. Guitton, J. A. Johannessen, V. Kerbaol and M. W. Hansen (2012), On the use of Doppler Shift for sea surface wind retrieval from SAR, *IEEE Trans. Geosci. Remote Sens.*, *50*(7), 2901–2909.

Ninnis, R. M., W. J. Emery, and M. J. Collins (1986), Automated extraction of pack ice motion from advanced very high resolution radiometer imagery, *J. Geophys. Res.*, *91*, 10,725–10,734.

Nouguier, F., C. A. Guèrin, and B. Chapron (2009), Choppy wave model for nonlinear gravity waves, *J. Geophys. Res.*, *114*, C09012, doi:10.1029/2008JC004984.

Plant, J. W. (2002), A stochastic, multiscale model of microwave backscatter from the ocean, *J. Geophys. Res.*, *107*(C9), 3120, doi:10.1029/2001JC000909.

Plant, W. J., and W. Alpers (1994), An Introduction to SAXON-FPN, *J. Geophys. Res.*, *99*, 9699–9703.

Portabella, M., and A. Stoffelen (2006), Scatterometer backscatter uncertainty due to wind variability, *IEEE Trans. Geosci. Remote Sens.*, *44*, 3356–3362.

Quazi, A. (1981), An overview on the time delay estimate in active and passive systems for target localization, *IEEE Trans. Acoust. Speech Signal Process*, *29*(3), 527–533, doi:10.1109/TASSP.1981.1163618.

Raney, R. K. (1986), Doppler properties of radars in circular orbits, *Int. J. Remote Sens.*, *7*(9), 1153–1162.

Romeiser, R., and D. R. Thompson (2000), Numerical study on the along-track interferometric radar imaging mechanism of oceanic surface currents, *IEEE Trans. Geosci. Remote Sens.*, *38*(1), 446–458.

Tagawa, N., T. Moriya, K. Iwashita, and M. Yoshizawa (2004), Multiplexed dual-chirp pulse compression method for ultrasonography, in *Ultrasonics Symposium*, 2004, vol. 3, pp. 2302–2305, IEEE, 23–27 Aug, doi:10.1109/ULTSYM.2004.1418301.

Thorndike, A. S., and R. Colony (1982), Sea ice motion in response to geostrophic winds, *J. Geophys. Res.*, *87*, 5845–5852.

Tokmakian, R., T. P. Strub, and J. McClean-Padman (1990), Evaluation of the maximum cross-correlation method of estimating sea surface velocities from sequential satellite images, *J. Atmos. Oceanic Technol.*, *7*(6), 852–865.

Vachon, P. W., and J. Wolfe (2011), C-band cross-polarization wind speed retrieval, *IEEE Geosci. Remote Sens. Lett.*, *8*, 456–458.

Van Zadelhoff, G.-J., A. Stoffelen, P. W. Vachon, J. Wolfe, J. Horstmann, and M. Belmonte Rivas (2013), Scatterometer hurricane wind-speed retrievals using cross-polarization, *Atmos. Meas. Tech. Discuss.*, *6*, 7945–7984.

Van Zadelhoff, G.-J., A. Stoffelen, P. W. Vachon, J. Wolfe, J. Horstmann, and M. Belmonte Rivas (2014), Retrieving hurricane wind speeds using cross polarization C-band measurements, *Atmos. Meas. Tech.*, *7*, 437–449.

Verhoef, A., M. Portabella, A. Stoffelen, and H. Hersbach, (2008), CMOD5.n: The CMOD5 GMF for neutral winds, *OSI SAF Rep. SAF/OSI/CDOP/KNMI/TEC/TN/165*, Koninklijk Nederlands Meteorologisch Instituut, technical report. [Available at http://www.knmi.nl/scatterometer/publications/.]

Verhoef, A., M. Portabella, and A. Stoffelen (2012), High-resolution ASCAT scatterometer winds near the coast, *IEEE Trans. Geosci. Remote Sens.*, *50*(7), 2481–2487, doi:10.1109/TGRS.2011.2175001.

Vogelzang, J., A. Stoffelen, A. Verhoef, J. de Vries, and H. Bonekamp (2009), Validation of two-dimensional variational ambiguity removal on SeaWinds scatterometer data, *J. Atmos. Oceanic Technol.*, *7*(26), 1229–1245, doi:10.1175/2008JTECHA1232.1.

Voronovich, A. (1994), Small-slope approximation for electromagnetic wave scattering at a rough interface of two dielectric half-spaces, *Waves Random Complex Media*, *4*(3), 337–367.

Wang H., J. Zhu, M. Lin, X. Huang, Y. Zhao, C. Chen, Y. Zhang, and H. Peng (2013), First six months quality assessment of HY-2A SCAT wind products using in situ measurements, *Acta Oceanol. Sin.*, *32* 27–33.

Zhang, B., W. Perrie, P. Vachon, J. A. Zhang, E. W. Uhlhorn, and Y. He (2014), High resolution hurricane vector winds from C-band dual-polarization SAR observations, *J. Atmos. Oceanic Technol.*, *31*, 272–286.

Zhang, Z., Y. Lu, and H. Hsu (2007), Detecting ocean currents from satellite altimetry, satellite gravity and ocean data, in *Dynamic Planet, International Association of Geodesy Symposia*, edited by P. Tregoning, and C. Rizos, Springer, Berlin.